

HST/COS Observations of Quasar Outflows in the 500 – 1050 Å Rest Frame: VII
Distances and Energetics for 11 Outflows in Five Quasars*

TIMOTHY R. MILLER,¹ NAHUM ARAV,¹ XINFENG XU,¹ GERARD A. KRISS,² AND RACHEL J. PLESHA²

¹*Department of Physics, Virginia Polytechnic Institute and State University, Blacksburg, VA 24061, USA*

²*Space Telescope Science Institute, 3700 San Martin Drive, Baltimore, MD 21218, USA*

ABSTRACT

From Hubble Space Telescope/Cosmic Origins Spectrograph spectra of five quasars, 16 outflows are detected. For 11 outflows, we are able to constrain their distances to the central source (R) and their energetics. In instances of multiple electron number density determinations (used in the calculation of R) for the same outflow, the values are consistent within errors. For the 11 outflows, eight have measurements for R (between 10 and 1000 pc), one has a lower limit, another has an upper limit, and the last has a range in R . There are two outflows that have enough kinetic luminosity to be major contributors to active galactic nucleus feedback. The outflowing mass is found primarily in a very high-ionization phase, which is probed using troughs from, e.g., Ne VIII, Na IX, Mg X, and Si XII. Such ions connect the physical conditions of these ultraviolet outflows to the X-ray warm absorber outflows seen in nearby Seyfert galaxies. The ion Cl VII and several new transitions from Ne V have been detected for the first time.

Keywords: Galaxy kinematics (602); Active galaxies (17); Broad-absorption line quasar (183); Interstellar absorption (831); Quasar absorption line spectroscopy (1317); Active galactic nuclei (16); Quasar (1319)

1. INTRODUCTION

Outflowing material from the centers of quasars can manifest as blueshifted absorption troughs in the rest frame of quasar spectra. Upward of 40% (Hewett & Foltz 2003; Dai et al. 2008; Ganguly & Brotherton 2008; Knigge et al. 2008) of the quasar population contains absorption outflows. These outflows are candidates for major feedback processes within active galactic nuclei (AGNs) as detailed in section 1 of Arav et al. (2020, hereafter Paper I) and references therein.

The kinetic luminosity (\dot{E}_K) of these outflows is the key quantity needed to assess the potential they have to produce the feedback processes. \dot{E}_K is linearly dependent on the distance from the central source (R), which can be inferred by simultaneously determining the electron number density (n_e) and ionization parameter (U_H) of the outflow (see section 7.1 of Arav et al. 2018). Around 30 such distances are currently found within the literature using this method (e.g., Paper I and references therein). Accretion disk wind models predict these outflows to reside around $R = 0.03$ pc (e.g., Murray et al. 1995; Proga et al. 2000; Proga & Kallman

2004), but the range found in the literature is between parsecs to tens of kiloparsecs.

The aforementioned feedback potential is determined by the ratio of the kinetic luminosity with respect to the Eddington luminosity. Hopkins & Elvis (2010) and Scannapieco & Oh (2004) require ratios exceeding 0.5% and 5%, respectively, for sufficient feedback. Of the outflow systems, 10 are currently known in the literature to meet at least one of these criteria. (Moe et al. 2009; Arav et al. 2013; Borguet et al. 2013; Chamberlain & Arav 2015; Xu et al. 2019, 2020a,c; Miller et al. 2020a).

The data analyzed here are part of a spectroscopic survey taken during Cycle 24 (GO-14777, PI: N. Arav). There are 10 quasars in total with redshifts around 1. The survey aimed to probe the 500-1050 Å rest-frame wavelength range (EUV500). The goal was to identify and measure diagnostic troughs (examples listed in Arav et al. 2013) capable of yielding outflow properties such as n_e as well as troughs that arise from very high-ionization potential ions (e.g. Ne VIII and Mg X), like those typically seen in X-ray warm absorbers (e.g., Reynolds 1997; Kaastra et al. 2000; Crenshaw et al. 2003; Kaastra et al. 2014). Such very high-ionization potential ions could establish a connection between X-ray warm absorbers and ultraviolet (UV) AGN outflows (Arav et al. 2013). A previous publication (Miller et al. 2018) details the results for the lowest redshift object where its highest-ionization potential ion is O VI.

* Based on observations with the NASA/ESA Hubble Space Telescope obtained at the Space Telescope Science Institute, which is operated by the Association of Universities for Research in Astronomy, Incorporated, under NASA contract NAS5-26555.

This paper is part of a series of publications describing the results of Hubble Space Telescope (HST) program GO-14777.

Paper I summarizes the results for the individual objects and discusses their importance to various aspects of quasar outflow research.

Paper II (Xu et al. 2020a) gives the full analysis for four outflows detected in SDSS J1042+1646, including the largest \dot{E}_k (10^{47} erg s $^{-1}$) outflow measured to date at $R = 800$ pc, and another outflow at $R = 15$ pc.

Paper III (Miller et al. 2020a) analyzes four outflows detected in 2MASS J1051+1247, which show remarkable similarities, are situated at $R \sim 200$ pc, and have a combined $\dot{E}_k = 10^{46}$ erg s $^{-1}$.

Paper IV (Xu et al. 2020b) presents the largest velocity shift and acceleration measured to date in a broad absorption line (BAL) outflow.

Paper V (Miller et al. 2020b) analyzes two outflows detected in PKS J0352-0711, including one outflow at $R = 500$ pc and a second outflow at $R = 10$ pc that shows an ionization potential-dependent velocity shift for troughs from different ions.

Paper VI (Xu et al. 2020c) analyzes two outflows detected in SDSS J0755+2306, including one at $R = 220$ pc with $\dot{E}_k = 10^{46}$ erg s $^{-1}$.

Paper VII is this work.

This paper is structured as follows. Section 2 describes the observations taken by the HST/Cosmic Origins Spectrograph (COS; Green et al. 2012) for the remaining five quasars of the survey. The spectral fitting for the unabsorbed continuum and emission lines is also discussed. Section 3 details the ionic column density and electron number density measurements in addition to the photoionization modeling. Comments on the individual outflows are given in Section 4. The physical properties, distances, and energetics of each outflow are given in section 5. A discussion of these results is in Section 6 with a summary and conclusions in section 7. In this paper, we adopt a cosmology with $h = 0.696$, $\Omega_m = 0.286$, and $\Omega_\Lambda = 0.714$, and we use Ned Wright’s Javascript Cosmology Calculator website (Wright 2006).

2. OBSERVATIONS, DATA REDUCTION, AND SPECTRAL FITTING

Table 1 contains the details of each observation as well as the coordinates, redshifts, and $E(B-V)$ values for the five quasars: SDSS J093602.10+200542.9, 7C 163119.39+393037.00, UM 425, 2MASS J14362129+0727208, and VV2006 J132957.2+540506. Miller et al. (2018) details the data processing steps, and each spectrum was corrected for Galactic extinction with the corresponding $E(B-V)$ values (Schlafly & Finkbeiner 2011). Figure 1 shows the dereddened, one-dimensional spectrum in black with errors in gray for each quasar. Individual outflow systems and corresponding absorption troughs are delineated S1, S2, S3, etc., in order of increasing absolute centroid velocities as summarized in Table 2,

which also contains the widths of the widest trough for each system. The slanted, dark green lines mark intervening hydrogen absorption systems identified by at least two hydrogen Lyman line transitions. The trough labels combine multiple transitions with wavelength separations less than 0.5 \AA into a single transition. Table 3 of Paper II provides a list of transition atomic data.

We fit the unabsorbed line and continuum emission in the same way as in Miller et al. (2018) and Xu et al. (2018). Specifically, a power law was used to fit the continuum emission while Gaussian profiles were used to fit line emission features, constrained by the red side of each line. Each emission line had the Gaussian centroid fixed at the rest-frame wavelength. For regions where a partial Lyman limit exists, the continuum was manually fitted with a cubic spline blueward of each limit, accounting for the decreased flux. The adopted, unabsorbed emission model is shown as the solid red contour in Figure 1 for each quasar.

3. DATA ANALYSIS

3.1. Ionic Column Density

From the analysis steps in Paper II, we first followed step 1 of the Synthetic Spectral Simulation (SSS) method to determine which troughs yield reliable ionic column density measurements (N_{ion}). The two methods used to obtain each measurement are the apparent optical depth (AOD) and partial covering (PC) methods (see e.g., Savage & Sembach (1991) and Arav et al. (2008) for each method, respectively). The AOD method is used to measure N_{ion} from a single ionic transition, typically yielding lower or upper limits. The PC method uses two ionic transitions from the same ion and energy level to yield an N_{ion} measurement for one ionic energy state.

The total column density of each ion (listed in Table 3 for each outflow) is the sum of all ionic energy states. In Table 3, red denotes upper limits while blue marks lower limits. The ratio of the adopted column densities to the best-fit, model predicted column densities are in the last column (see Section 3.2 and Figure 2). Ratios greater than one are expected for upper limits and vice versa for lower limits.

The same criteria from Paper II are used to determine measurements, upper limits, and lower limits. All PC determined N_{ion} are treated as measurements, and N_{ion} for troughs where both $0.05 < \tau_{\text{max}} < 0.5$ and where troughs from ions of similar ionization potential have $\tau_{\text{max}} > 2$ are also treated as measurements. N_{ion} measured from regions where no trough is identified (a maximum optical depth, τ_{max} , less than 0.05) are upper limits. Our adopted values are the PC values when available and AOD values otherwise. The adopted errors include a systematic error (20% of the adopted value), which is added in quadrature to the corresponding AOD/PC errors (see Table 3). This systematic error accounts for uncertainties in the unabsorbed emission model (e.g., Miller et al. 2018; Xu et al. 2018).

Table 1. HST/COS observations, coordinates, redshifts, and Galactic $E(B-V)$ values for the five quasars.

Object	SDSS J0936+2005	UM 425	VV2006 J1329+5405	2MASS J1436+0727	7C 1631+3930
J2000 R.A.	09:36:02.11	11:23:20.73	13:29:57.15	14:36:21.30	16:33:02.10
J2000 Decl.	+20:05:42.90	+01:37:47.50	+54:05:05.90	+07:27:20.89	+39:24:27.4
Redshift (z)	1.1832	1.4720	0.9496	0.8944	1.0246
Galactic $E(B-V)$	0.0267	0.0313	0.0128	0.0244	0.0070
HST/COS Grating G130M					
Observation date	2017 Nov 21	2017 Nov 15	2017 Sep 30	2017 Jul 17	2017 May 13
Exposure time (s)	4360	3870	3690	4130	4200
Observed range (\AA)	1155–1460	1130–1470	1130–1470	1130–1470	1130–1470
Rest-frame range (\AA)	520–670	460–595	580–755	600–775	560–725
HST/COS Grating G160M					
Observation date	2017 Nov 22	2017 Nov 15–16	2017 Sep 30	2017 Jul 17	2017 May 14
Exposure time (s)	4660	4660	4660	4660	5200
Observed range (\AA)	1405–1800	1405–1800	1405–1800	1405–1800	1380–1765
Rest-frame range (\AA)	645–825	570–730	720–920	740–950	695–890

Table 2. Detected Outflows in each quasar.

Outflow System	Centroid Velocity (km s ⁻¹)	FWHM (km s ⁻¹)
SDSS J0936+2005		
S1	-7960	200
S2	-8200	400
S3	-9300	350
UM 425		
S1	-1640	400
S2	-1980	200
S3	-2200	200
S4	-9420	300
VV2006 J1329+5405		
S1	-11600	1450
S2	-12900	600
2MASS J1436+0727		
S1	-14400	300
7C 1631+3930		
S1	-1010	200
S2	-1430	550
S3	-5300	150
S4	-5770	250
S5	-6150	150
S6	-7210	200

3.2. Photoionization Modeling

The ionization equilibrium of a quasar outflow is dominated by photoionization. Therefore, the outflow is characterized by its total hydrogen column density (N_{H}) and U_{H} . These two values together are the photoionization solution for each outflow, where the best-fit photoionization solution is determined from grids of photoionization models generated by the code Cloudy (Ferland et al. 2017, version c17.00). Each component of an outflow system is modeled with one N_{H} and U_{H} . The grid containing the best-fit solution assumes one of two metallicities and the spectral energy distribution (SED) HE0238 SED (Arav et al. 2013), which has a similar rest-frame wavelength range to our objects. The two metallicities are solar, Z_{\odot} , from Grevesse et al. (2010) and super-solar, $Z = 4.68Z_{\odot}$, from Paper V. Only the solutions for VV2006 J1329+5405 used the super-solar value (see section 4.3).

To determine the best-fit solution, we follow the remaining steps of the SSS method as outlined here. We obtain preliminary values for N_{H} and U_{H} from the measured N_{ion} that are known to be uncontaminated (a subset of the values in Table 3). This preliminary photoionization solution and subsequent solutions are found through χ^2 -minimization, corresponding to the minimum of the merit function given in equation 4 of Borguet et al. (2012). Then a model spectra (see section 3.3 of Paper II for construction details) containing all outflows

for each quasar is created and compared to the observed spectra. New upper/lower limits and measurements are assessed and used to further constrain the values of N_{H} and U_{H} . A best-fit photoionization solution is generated after a few iterations of this process. Figure 2 shows these best-fit photoionization solutions for each outflow, which were constrained by all total N_{ion} values in Table 3.

The colored contours for individual ions in Figure 2 show the N_{H} and U_{H} values where the model N_{ion} are within 1σ of the observed values, assuming the HE0238 SED and solar metallicity (super-solar metallicity for VV2006 1329+5405). Solid contours represent N_{ion} measurements while dotted and dashed lines indicate upper and lower limits, respectively. The adopted best-fit solution is the solid black dots and 1σ error ellipses. A two phase photoionization solution (e.g., Arav et al. 2013, Paper II; Paper III; Paper V), comprised of a high-ionization phase (HP) and very high-ionization phase (VHP), is needed for 10 of the 16 outflow systems. The remaining six require only a single phase solution (one VHP). The values for all N_{H} and U_{H} determinations are given in Table 4. Comments on individual objects can be found in section 4.

3.3. Electron Number Density Determination

All of the excited-state troughs shown in Figure 1 become populated primarily through electron collisions, where the collision frequency and energy transferred depend on n_e and the electron temperature. Therefore, the relative populations between an excited-state and a ground state from the same ion can be used to calculate n_e (e.g., de Kool et al. 2001; Hamann et al. 2001; de Kool et al. 2002; Korista et al. 2008). To calculate the necessary population ratios, which is equal to the column density ratios, we used the CHIANTI 8.0.7 database (Dere et al. 1997; Landi et al. 2013) as was done in previous works (e.g., Borguet et al. 2012b; Arav et al. 2013, 2015, 2018; Chamberlain & Arav 2015). Separate discussions follow for each quasar, with the results shown in Figure 3 where the theoretical column density ratios as a function of n_e are shown with the black contours for each population ratio at the temperature of the first outflow listed in each panel. The top axis shows the distance scale obtained from equation 1 for this outflow as well. The measured column density ratios with uncertainties for each outflow system are overlaid, and the individual column densities are listed in Table 3.

4. COMMENTS ON INDIVIDUAL OUTFLOWS

4.1. SDSS J0936+2005

S1: The photoionization solution consists of two phases. A single phase solution at the intersection of Ar VIII and Mg X overpredicts the N_{ion} of Ne VIII by a factor of 10, requiring this two phase solution. The VHP is constrained primarily by the N_{ion} measurements of Ne VIII and Mg X as well as an upper limit on Al XI

while the HP has only upper and lower limit constraints. The VHP contains four times more hydrogen column density than the HP.

The only detected troughs with useful n_e diagnostics for S1 are from Ne v and Ne vi. The Ne v* 569.83 Å trough is deeper than the Ne v 568.42 Å trough. Conversely, the Ne vi* 562.81 Å trough is shallower than the Ne vi 558.60 Å trough. These facts already predict that the n_e of S1 is above the critical density for the energy level associated with the Ne v* 569.83 Å transition (413 cm^{-1}) and below that of the Ne vi* 562.81 Å transition (1307 cm^{-1}).

The majority of the N_{ion} for Ne v and Ne vi come from the HP. Therefore, the total N_{ion} of each can be constrained from the HP solution in the same way as was done in section 3.3 of Paper III. Specifically, the deeper trough is assumed to contain the missing column density needed for the total to match the value constrained by the photoionization solution. Paper III showed that the shallower trough N_{ion} does not increase significantly when considering maximum saturation effects, making this assumption acceptable. From there, a measured ratio from the N_{ion} of Ne vi* and Ne vi is obtained. We are left with a lower limit for Ne v. This happens because there is another excited energy level of Ne v (1111 cm^{-1}) that would also be populated, but the transitions needed to probe the level are blended with the geocoronal Ly α emission line. Since we do not know the relative trough depths of the excited levels, we cannot determine if the observed Ne v* 569.83 Å trough is the deepest. Therefore, the adopted value for n_e is from the Ne vi diagnostic, which is also consistent within errors with the lower limit determined from the Ne v diagnostic.

S2: A two phase photoionization solution is needed since a single phase solution at the intersection of Ca vi and Al xi overpredicts the column densities of Ca x (by a factor of 100) and Ar viii (by a factor of 10). The HP is bounded by the N_{ion} measurement of Ar viii and the upper and lower limits of S iv and Ca vi, respectively. The VHP is constrained by the column density measurements of Na ix and Al xi along with the upper limit from Ca x. The N_{ion} from Al xi 550 Å is treated as a measurement even though we measure only a single trough since it is well defined and much shallower than the Mg x troughs, which have a similar ionization potential to Al xi. We assume since the ionization potentials are similar that they should be produced in the same regions of the outflow and have the same covering solutions. The VHP carries 90% of the total hydrogen column density.

The troughs from the excited transitions of O iv are either heavily blended or show one-to-one trough depths with ground-state transitions, making them unsuitable for n_e measurements. However, the troughs from excited levels of Ne v and Ne vi can yield useful measurements. Like S1, the excited-state trough of Ne v is deeper than

its corresponding ground-state trough while the opposite is true for the Ne vi troughs. The majority of the N_{ion} for Ne v and Ne vi also comes from the HP. Therefore, the same method used for S1 to determine n_e is used for S2. Again, the adopted value for n_e is from the Ne vi diagnostic.

S3: The two phase solution contains only upper and lower limits where the HP is constrained by O iii, N iv, and Ne v while the VHP is bounded by Mg x, Ne viii, and Ne vi. Choosing a single phase solution where N iv crosses Ne viii overpredicts the upper limit of Ne v by a factor of 15. The VHP contains over 99% of the total hydrogen column density.

The only useful n_e diagnostic comes from the transitions of Ne vi, where the majority of the N_{ion} resides in the VHP. The same process as was used for S1 and S2 yields the n_e measurement for S3.

4.2. UM 425

S1: A well constrained two phase photoionization solution is determined from the N_{ion} constraints. Like S2 of SDSS J0936+2005, the N_{ion} of Al xi is treated as a measurement since the 550 Å trough is shallow compared to the Mg x and Si xii troughs (all three have similar ionization potentials and therefore have similar assumed origins and covering solutions within the outflow) and the trough is well defined. About 98% of the total N_{H} is contained within the VHP.

The O iv and O iv* transitions are quite blended, preventing usable n_e estimates. The S iv and S iv* troughs are also only upper limits. This leaves the transitions from Ne v and Ne vi. The Ne v* 482.99 Å trough is not well defined, and the Ne v* 481.35 Å is blended with an intervening system and other absorption, leading to unreliable N_{ion} measurements for both troughs. However, an upper limit and measurement for n_e is obtained from the Ne v* 572.30 Å and Ne v* 569.83 Å N_{ion} , respectively, along with the ground-state column density of Ne v, which is constrained by the HP since it carries the majority of the N_{ion} for Ne v. For the Ne vi troughs, the Ne vi* 562.81 Å trough is severely blended with an intervening system, preventing an n_e estimate. Therefore, the n_e measurement using the Ne v* 569.83 Å diagnostic is adopted as the best value.

S2: There is a two phase solution with an unbounded VHP. Unlike S1, the Al xi 550 Å trough is not well defined so we do not take it as a measurement nor a lower limit since it is uncertain if the absorption arises from intervening systems. The VHP carries at least 93% of the total N_{H} .

Like S1, the O iv and O iv* transitions are blended, and the S iv and S iv* transitions are upper limits. Therefore, neither species is usable for n_e estimates. The Ne v* 481.35 Å and 572.30 Å as well as the Ne vi* 562.81 Å troughs do not yield accurate N_{ion} as they are blended with intervening systems and other absorption. However, S2 does have two consistent n_e measurements

where the ground-state column density is constrained by the HP: one from the N_{ion} ratio of Ne v* 569.83 Å and the ground-state and another from the N_{ion} ratio of Ne v* 482.99 Å and the ground state. Since the Ne v* 569.83 Å trough is better defined than the Ne v* 482.99 Å trough and lies within a portion of the spectrum with less unaccounted for absorption that may lead one to question the identification of the absorption trough, we choose the n_e value determined from the Ne v* 569.83 Å and ground-state diagnostic as the best value.

S3: There is an unbounded VHP and bounded HP. Like in the case of S2, the Al xi 550 Å trough is unreliable as a measurement or a lower limit. The errors allow for both phases to carry equal amounts of the total hydrogen column density.

The O iv and O iv* transitions as well as the S iv and S iv* transitions are upper limits and therefore cannot yield n_e estimates. The only excited trough that is not severely blended is the Ne v* 572.30 Å transition. From the N_{ion} ratio of Ne v* 572.30 Å and the ground state (constrained by the HP), we determine an n_e measurement.

S4: A two phase solution exists with a bounded HP and VHP. The Al xi 550 Å trough is treated as a lower limit since it has a similar depth to the Mg x and Si xii troughs. The VHP contains the majority of the total N_{H} at 90%.

The only useful n_e estimates arise from the Ne v* 482.99 Å, Ne v* 569.83 Å (blended on the blue side with an intervening system), and Ne vi* 562.81 Å troughs. The first two yield electron number density lower limits since they are deeper than the Ne v 480.42 Å (blended on the red side with an intervening system), resulting in ratios that are consistent with the theoretical limit. For Ne vi, the Ne vi* 562.81 Å trough is blended with unidentified absorption, preventing an n_e estimate. The lower limit obtained from the Ne v* 482.99 Å diagnostic is adopted as the best value since it provides a tighter constraint compared to the other lower limit.

4.3. VV2006 J1329+5405

S1: The photoionization solution uses the super-solar value since solar values yield a solution that overpredicts the hydrogen N_{ion} upper limit by more than a factor of five. The two phase solution has an unbounded VHP, which carries around 90% of the total N_{H} .

Two lower limits and one upper limit on n_e are determined for S1. First, the O iv* 790.11 Å trough is free from major contamination or blending, but can only yield a lower limit since it shows a one to one trough depth with the uncontaminated red side of the O iv 787.71 Å and blue side of the O iv 608.40 Å troughs. Therefore, using the HP to constrain the total N_{ion} of O iv, a lower limit on n_e is obtained. Second, the O v* multiplet near 730 Å in the quasar rest frame is quite blended, but the red half of the O v* 762.00 Å trough

is not blended. However, the trough is likely saturated as it shows a one to one trough depth with the O v* 760.45 Å trough, whose transition is from the same energy level and has a larger oscillator strength. Therefore, a lower limit to the N_{ion} of O v* 762.00 Å trough is estimated by doubling the N_{ion} measured from the red half of the trough. Using the HP solution to constrain the total N_{ion} of O v along with this lower limit yields the other lower limit to n_e . Third, an upper limit to the N iv* 923.22 Å trough is measured, and the total N_{ion} for N iv is constrained by the HP. Together, an n_e upper limit is calculated. The lower limit n_e determined from the O v diagnostic and upper limit from the N iv diagnostic are adopted as the best range since they provide the tightest constraints on n_e .

S2: For consistency, S2 also used the super-solar value, but a solar metallicity solution is equally viable. It contains a single VHP with the possibility of an HP if its $\log(U_{\text{H}})$ is less than 0 and total hydrogen column density is below the O iv upper limit.

The O v* multiplet is highly blended with intervening systems. Similarly, the O iv* 790.11 Å trough is blended with troughs from S1. Therefore, n_e cannot be constrained, leaving the distance unknown.

4.4. 2MASS J1436+0727

S1: The only detected trough is Ne viii, yielding a bounded VHP solution with the aid of upper limit constraints from H i and O v. An HP solution could exist for N_{H} values below the O v upper limit and U_{H} smaller than the VHP. The outflow has no N_{ion} lower limits or measurements from ground-state transitions with possible excited levels nor any excited level transitions, rendering an n_e estimate indeterminable.

4.5. 7C 1631+3930

S1: A single phase (VHP) is detected. An HP could exist following similar requirements of previously discussed single phase outflows.

Only upper limits to excited-state N_{ion} are measured, which at best will result in n_e upper limits. These N_{ion} upper limits are typically accompanied by upper limits on the ground-state N_{ion} as well, yielding no constraint on n_e . However, the VHP solution contains a large amount of Ne vi that would be detected if the spectrum covered the Ne vi 558.60 Å trough. Therefore, an upper limit to n_e is determined from the upper limit N_{ion} of the Ne vi* 562.81 Å and the ground-state N_{ion} of Ne vi (determined by subtracting the upper limit from the total column density of Ne vi constrained by the VHP).

S2: A VHP and an HP are needed following similar arguments as was shown for the outflows in SDSS J0936+2005. Like S3 of SDSS J0936+2005, the overwhelming majority (98%) of the hydrogen column density is contained within the VHP.

For n_e determinations, S2 has an upper limit N_{ion} for the Ne v* 572.30 Å trough and a measurement for the Ne v* 569.83 Å trough since this trough is much shallower than the Ne v 568.42 Å trough. The HP also contains the majority of the Ne v column density, yielding an n_e upper limit from the Ne v* 572.30 Å and ground-state column density ratio and a measurement from the N_{ion} ratio of Ne v* 569.83 Å and the ground state. The adopted n_e is the value determined by the Ne v* 569.83 Å and ground-state diagnostic.

S3: Similar to S1, only a VHP is needed to explain the detected troughs, and an HP could exist following similar requirements as discussed previously. The VHP solution is unbounded, allowing solutions beyond $\log(U_{\text{H}}) = 2$ and $\log(N_{\text{H}}) = 23.5$. There are not any useful n_e diagnostics for this outflow.

S4: Like S2, a two phase solution explains the observed column density constraints, and the VHP contains 96% of the total N_{H} . Similar to S1, an n_e measurement is obtained from the N_{ion} ratio of the observed Ne v* 572.30 Å trough and the total N_{ion} constrained by the HP (the ground-state trough is outside the observed wavelength range like in the case of S1).

S5 and S6: A single VHP is detected in both outflows with possible HPs existing below each N IV upper limit and $\log(U_{\text{H}}) < 0$. Neither outflow has useful n_e diagnostics, leaving their distances unconstrained.

5. RESULTS

5.1. Outflow Distance, Energetics, and Properties

The ionization parameter relates the distance of each outflow from the central source to other measurable properties:

$$U_{\text{H}} = \frac{Q_{\text{H}}}{4\pi R^2 n_{\text{H}} c} \quad (1)$$

where n_{H} is the hydrogen number density ($n_e \approx 1.2n_{\text{H}}$ for highly ionized plasma), R is the distance from the central source, c is the speed of light, and Q_{H} is the incident ionizing photon rate of hydrogen. Taking the HE0238 SED and integrating for energies above 1 Ryd yields the Q_{H} values in Table 4, which also contains the distances of each outflow. This integration process includes the methodology of Hogg (1999) for calculating the luminosity distance and applying the k -correction to the observed flux.

From Borguet et al. (2012), the average mass flow rate and kinetic luminosity over a dynamical timescale (R/v) for a partially filled, thin shell outflow are given by

$$\dot{M} \simeq 4\pi\Omega R N_{\text{H}} \mu m_p v \quad (2)$$

and

$$\dot{E}_{\text{K}} \simeq \frac{1}{2} \dot{M} v^2 \quad (3)$$

where $\Omega = 0.4^{+0.14}_{-0.14}$ is the global covering factor (the fraction of quasars with observed Ne VIII mini-BAL outflows; Muzahid et al. 2013), R is the distance from the

central source, $\mu = 1.4$ is the mean atomic mass per proton, N_{H} is the hydrogen column density, m_p is the proton mass, and v is the outflow velocity. Table 4 contains the calculated energetics for each outflow assuming the HP and VHP have the same global covering factor, and the hydrogen column density value used for the energetics is the sum of the N_{H} from each phase.

Table 3. Total Ionic Column Densities

Ion	AOD ^a (10 ¹² cm ⁻²)	PC ^a (10 ¹² cm ⁻²)	Adopted ^b (10 ¹² cm ⁻²)	Adopted ^c Best Model
SDSS J0936+2005				
S1: $v = -7960 \text{ km s}^{-1}$				
N IV	48 ⁺¹² ₋₁₀	...	>48 ₋₁₄	>0.99 _{-0.29}
O IV	250 ⁺⁷⁰ ₋₆₀	...	<250 ⁺⁸⁰	<0.99 ^{+0.34}
O V	220 ⁺²⁰ ₋₁₀	...	>220 ₋₅₀	>0.06 _{-0.01}
Ne v	550 ⁺⁸⁰ ₋₇₀	...	>550 ₋₁₃₀	>0.67 _{-0.16}
Ne v* ^d	390 ⁺⁷⁰ ₋₅₀	...	>390 ₋₁₀₀	...
Ne v ^e	160 ⁺⁵⁰ ₋₄₀	...	160 ⁺⁶⁰ ₋₅₀	...
Ne VI	2000 ⁺¹²⁰ ₋₁₀₀	...	>2000 ₋₄₂₀	>0.57 _{-0.12}
Ne VI* ^f	730 ⁺⁷⁰ ₋₇₀	...	730 ⁺¹⁶⁰ ₋₁₆₀	...
Ne VI ^e	1290 ⁺⁹⁰ ₋₈₀	...	6690 ⁺³⁸¹⁰ ₋₂₀₄₀	...
Ne VIII	1900 ⁺²⁴⁰ ₋₁₉₀	2200 ⁺⁴⁷⁰ ₋₂₃₀	2200 ⁺⁶⁵⁰ ₋₅₁₀	1.00 ^{+0.24} _{-0.22}
Na IX	140 ⁺³⁰ ₋₃₀	...	<140 ⁺⁵⁰	<2.32 ^{+0.73}
Mg X	1500 ⁺¹⁴⁰ ₋₁₃₀	2400 ⁺⁴⁴⁰ ₋₂₄₀	2400 ⁺⁶⁵⁰ ₋₅₃₀	1.00 ^{+0.27} _{-0.22}
Al XI	190 ⁺⁶⁰ ₋₇₀	...	<190 ⁺⁷⁰	<1.04 ^{+0.40}
S IV	10 ⁺² ₋₃	...	<10 ⁺³	<84.2 ^{+25.2}
Ar VI	43 ⁺¹⁵ ₋₁₁	...	<43 ⁺¹⁷	<3.53 ^{+1.39}
Ar VII	16 ⁺⁴ ₋₃	...	<16 ⁺⁵	<1.66 ^{+0.52}
Ar VIII	25 ⁺¹¹ ₋₁₁	...	<25 ⁺¹²	<1.08 ^{+0.52}
Ca VI	110 ⁺⁷⁰ ₋₅₀	...	<110 ⁺⁸⁰	<3.87 ^{+2.78}
Ca VIII	160 ⁺⁷⁰ ₋₅₀	...	<160 ⁺⁸⁰	<4.15 ^{+1.89}
Ca X	74 ⁺³ ₋₃₄	...	<74 ⁺¹⁵	<6.14 ^{+1.24}
S2: $v = -8200 \text{ km s}^{-1}$				
N IV	200 ⁺²⁰ ₋₂₀	...	>200 ₋₄₀	>0.09 _{-0.02}
O IV	1500 ⁺¹⁴⁰ ₋₁₂₀	...	>1500 ₋₃₂₀	>0.09 _{-0.02}
O V	710 ⁺⁴⁰ ₋₃₀	...	>710 ₋₁₅₀	>0.01 _{-0.002}
Ne v	3200 ⁺¹⁶⁰ ₋₁₃₀	...	>3200 ₋₆₅₀	>0.15 _{-0.03}
Ne v* ^d	1960 ⁺¹²⁰ ₋₁₀₀	...	>1960 ₋₄₁₀	...
Ne v ^e	1240 ⁺¹⁰⁰ ₋₈₀	...	1240 ⁺²⁷⁰ ₋₂₆₀	...
Ne VI	5900 ⁺²⁵⁰ ₋₂₀₀	...	>5900 ₋₁₂₀₀	>0.15 _{-0.03}
Ne VI* ^f	2420 ⁺¹³⁰ ₋₁₁₀	...	2420 ⁺⁵⁰⁰ ₋₅₀₀	...
Ne VI ^e	3450 ⁺²²⁰ ₋₁₆₀	...	29200 ⁺¹⁶²⁰⁰ ₋₁₁₇₀₀	...
Ne VIII	6800 ⁺⁵⁷⁰ ₋₄₀₀	...	>6800 ₋₁₄₀₀	>0.12 _{-0.02}
Na IX	1700 ⁺¹⁶⁰ ₋₁₄₀	1900 ⁺¹⁶⁰ ₋₁₁₀	1900 ⁺⁴²⁰ ₋₄₀₀	1.46 ^{+0.32} _{-0.30}
Mg X	6200 ⁺²⁹⁰ ₋₂₅₀	...	>6200 ₋₁₃₀₀	>0.26 _{-0.05}
Al XI	530 ⁺¹⁰⁰ ₋₉₀	...	530 ⁺¹⁴⁰ ₋₁₄₀	0.77 ^{+0.21} _{-0.20}
S IV	23 ⁺⁴ ₋₄	...	<23 ⁺⁶	<0.98 ^{+0.25}
Ar VI	91 ⁺²⁰ ₋₁₇	...	>91 ₋₂₅	>0.17 _{-0.05}

Table 3 continued

Table 3 (continued)

Table 3 (continued)

Ion	AOD ^a	PC ^a	Adopted ^b	Adopted ^c Best Model	Ion	AOD ^a	PC ^a	Adopted ^b	Adopted ^c Best Model
	(10 ¹² cm ⁻²)	(10 ¹² cm ⁻²)	(10 ¹² cm ⁻²)			(10 ¹² cm ⁻²)	(10 ¹² cm ⁻²)	(10 ¹² cm ⁻²)	
Ar VII	88 ⁺⁶ ₋₅	...	>88-18	>0.53-0.11	Na IX	280 ⁺⁷⁸ ₋₆₈	...	<280+96	<1.31+0.45
Ar VIII	210 ⁺³⁰ ₋₃₀	240 ⁺⁴⁰ ₋₃₀	240 ⁺⁶⁰ ₋₆₀	0.93 ^{+0.24} _{-0.23}	Mg X	3300 ⁺¹⁹⁰ ₋₁₇₀	...	>3300-680	>0.94-0.19
Ca VI	680 ⁺⁹⁰ ₋₉₀	...	>680-160	>1.18-0.28	S IV	13 ^{+3.7} _{-4.2}	...	<13+4.5	<5.83+2.02
Ca VII	1300 ⁺¹⁹⁰ ₋₁₇₀	...	<1300+320	<1.88+0.46	Ar V	25 ^{+6.9} ₋₁₁	...	<25+8.5	<1.02+0.35
Ca VIII	210 ⁺⁵⁰ ₋₅₀	...	<210+70	<1.16+0.39	Ar VII	14 ^{+2.1} _{-2.0}	...	<14+3.5	<1.00+0.25
Ca X	61 ⁺³⁹ ₋₂₇	...	<61+41	<0.48+0.32	Ca VII	140 ⁺⁶⁶ ₋₇₁	...	<140+71	<2.25+1.16
S3: v = -9300 km s ⁻¹					Ca X	36 ⁺¹³ ₋₁₃	...	<36+15	<1.01+0.41
N IV	93 ⁺¹⁶ ₋₁₄	...	>93-23	>1.08-0.27	S3: v = -2200 km s ⁻¹				
O III	110 ⁺³⁰ ₋₃₀	...	<110+40	<0.96+0.34	O V	360 ⁺¹⁹ ₋₁₆	...	>360-74	>0.10-0.02
O V	300 ⁺²⁰ ₋₂₀	...	>300-60	>0.37-0.08	Ne IV	260 ⁺⁶⁶ ₋₅₇	...	<260+84	<6.56+2.09
Ne V	120 ⁺⁶⁰ ₋₄₀	...	<120+60	<0.84+0.43	Ne V	830 ⁺⁵¹ ₋₄₈	...	>830-170	>1.00-0.21
Ne VI	1300 ⁺¹²⁰ ₋₁₁₀	...	>1300-280	>1.06-0.23	Ne v* ^g	230 ⁺³⁰ ₋₃₀	...	230 ⁺⁶⁰ ₋₅₀	...
Ne VI* ^f	530 ⁺⁷⁰ ₋₇₀	...	530 ⁺¹³⁰ ₋₁₃₀	...	Ne v ^e	600 ⁺⁴⁰ ₋₄₀	...	600 ⁺¹³⁰ ₋₁₃₀	...
Ne VI ^e	790 ⁺⁹⁰ ₋₈₀	...	790 ⁺⁸⁷⁰ ₋₁₈₀	...	Ne VI	1900 ⁺¹¹⁰ ₋₉₀	...	>1900-400	>0.78-0.16
Ne VIII	2300 ⁺³⁰⁰ ₋₂₄₀	...	>2300-530	>0.95-0.21	Na VI	140 ⁺⁶³ ₋₄₈	...	<140+69	<3.10+1.58
Na IX	48 ⁺²³ ₋₂₂	...	<48+25	<1.93+1.01	Na IX	320 ⁺⁷⁸ ₋₇₀	...	<320+100	<1.31+0.41
Mg X	350 ⁺¹⁰⁰ ₋₉₀	...	<350+120	<0.99+0.34	Mg X	4000 ⁺²⁰⁰ ₋₁₈₀	...	>4000-830	>0.66-0.14
Al XI	160 ⁺⁶⁰ ₋₇₀	...	<160+70	<34.3+15.5	Si XII	1100 ⁺⁹⁶ ₋₈₈	...	>1100-240	>0.97-0.21
S IV	24 ^{+3.6} _{-3.6}	...	<24+6.0	<1.79+0.45	Ar VI	20 ^{+19.2} _{-9.8}	...	<20+20	<1.05+1.02
Ar VI	46 ⁺¹⁹ ₋₁₅	...	<46+21	<67.9+31.0	Ar VII	15 ^{+2.6} _{-2.4}	...	<15+4.0	<1.80+0.47
Ar VII	9.2 ^{+3.7} _{-2.9}	...	<9.2+4.1	<10.0+4.47	Ca X	85 ⁺¹⁵ ₋₁₅	...	<85+23	<9.71+2.63
Ar VIII	25 ^{+9.0} ₋₁₀	...	<25+10	<8.62+3.55	S4: v = -9420 km s ⁻¹				
UM 425					O IV	250 ⁺⁴⁵ ₋₄₂	...	<250+66	<0.91+0.25
S1: v = -1640 km s ⁻¹					O V	330 ⁺¹⁶ ₋₁₅	...	>330-67	>0.04-0.01
O V	1300 ⁺⁷¹ ₋₄₄	...	>1300-260	>0.09-0.02	Ne V	1400 ⁺¹⁶⁰ ₋₁₃₀	...	>1400-320	>1.10-0.24
Ne IV	140 ⁺²⁶ ₋₂₄	...	<140+38	<0.99+0.27	Ne v* ^d	510 ⁺⁶⁰ ₋₆₀	...	>510-120	...
Ne V	3500 ⁺⁸⁹ ₋₈₁	...	>3500-710	>1.03-0.21	Ne v* ^g	770 ⁺¹³⁰ ₋₁₀₀	...	>770-70	...
Ne v* ^d	350 ⁺³⁰ ₋₃₀	...	350 ⁺⁸⁰ ₋₈₀	...	Ne v ^e	170 ⁺⁸⁰ ₋₅₀	...	170 ⁺⁹⁰ ₋₆₀	...
Ne v* ^g	80 ⁺²⁰ ₋₂₀	...	<80+30	...	Ne VI	3800 ⁺¹⁶⁰ ₋₁₄₀	...	>3800-780	>0.27-0.05
Ne v ^e	3180 ⁺⁸⁰ ₋₇₀	...	3180 ⁺⁷¹⁰ ₋₇₁₀	...	Na IX	650 ⁺¹²⁰ ₋₈₂	...	>650-150	>1.00-0.24
Ne VI	7300 ⁺⁴²⁰ ₋₂₇₀	...	>7300-1500	>0.74-0.15	Mg X	2500 ⁺⁷⁹ ₋₇₃	...	>2500-510	>0.08-0.02
Ne VII	12000 ⁺⁰ ₋₀	...	<12000+4000	<0.94+0.31	Al XI	2000 ⁺¹⁸⁰ ₋₁₆₀	...	>2000-420	>0.48-0.10
Na IX	2400 ⁺²⁶⁰ ₋₂₁₀	3900 ⁺¹⁴⁰⁰ ₋₆₀₀	3900 ⁺¹⁶⁰⁰ ₋₉₈₀	1.12 ^{+0.46} _{-0.28}	Si XII	7400 ⁺³¹⁰ ₋₂₈₀	...	>7400-1500	>0.12-0.02
Mg X	18000 ⁺¹⁰⁰⁰ ₋₆₇₀	...	>18000-3600	>0.12-0.02	P XIII	870 ⁺³²⁰ ₋₃₁₀	...	<870+370	<1.79+0.77
Al XI	1290 ⁺¹⁰⁰ ₋₁₀₀	...	1290 ⁺²⁸⁰ ₋₂₈₀	1.00 ^{+0.22} _{-0.22}	Ar VIII	190 ⁺⁴¹ ₋₃₉	...	<190+57	<3.86+1.13
Si XII	7300 ⁺²⁷⁰ ₋₂₂₀	...	>7300-1500	>0.05-0.01	Ca X	150 ⁺⁵² ₋₄₇	...	<150+60	<0.97+0.38
S IV	23 ⁺¹⁹ ₋₁₄	...	<23+20	<21.4+18.2	2MASS J1436+0727				
Ca VIII	100 ⁺⁴⁵ ₋₃₂	...	<100+49	<1.47+0.66	S1: v = -14400 km s ⁻¹				
S2: v = -1980 km s ⁻¹					H I	590 ⁺¹⁶⁰ ₋₁₉₀	...	<590+200	<6.30+2.14
O V	330 ⁺²⁰ ₋₁₆	...	>330-68	>0.04-0.01	O V	110 ⁺²¹ ₋₁₉	...	<110+30	<6.64+1.81
Ne IV	180 ⁺⁵¹ ₋₄₄	...	<180+63	<1.31+0.45	Ne VIII	2400 ⁺⁹⁷ ₋₉₁	2900 ⁺¹⁵⁰ ₋₁₂₀	2900 ⁺⁵⁹⁰ ₋₅₈₀	1.00 ^{+0.20} _{-0.20}
Ne V	1900 ⁺⁷¹ ₋₆₄	...	>1900-380	>1.01-0.20	Na IX	1600 ⁺¹⁷⁰ ₋₁₃₀	...	<1600+350	<10.6+2.31
Ne v* ^d	500 ⁺³⁰ ₋₃₀	...	500 ⁺¹¹⁰ ₋₁₁₀	...	VV2006 J1329+5405				
Ne v* ^g	270 ⁺⁵⁰ ₋₄₀	...	270 ⁺⁷⁰ ₋₇₀	...	S1: v = -11600 km s ⁻¹				
Ne v ^e	1080 ⁺⁴⁰ ₋₄₀	...	1080 ⁺²²⁰ ₋₂₂₀	...	H I	5100 ⁺¹⁴⁰⁰ ₋₁₂₀₀	...	<5100+1700	<1.23+0.42
Ne VI	2000 ⁺¹⁴⁰ ₋₁₂₀	...	>2000-420	>0.39-0.08	N IV	560 ⁺¹² ₋₁₁	...	>560-110	>0.18-0.04

Table 3 continued

Table 3 continued

Table 3 (continued)

Table 3 (continued)

Ion	AOD ^a	PC ^a	Adopted ^b	Adopted ^c Best Model	Ion	AOD ^a	PC ^a	Adopted ^b	Adopted ^c Best Model
	(10 ¹² cm ⁻²)	(10 ¹² cm ⁻²)	(10 ¹² cm ⁻²)			(10 ¹² cm ⁻²)	(10 ¹² cm ⁻²)	(10 ¹² cm ⁻²)	
N IV ^{*h}	190 ⁺⁵⁰ ₋₄₀	...	<190 ⁺⁶⁰	...	Ne V ^{*g}	130 ⁺⁴⁰ ₋₃₀	...	<130 ⁺⁵⁰	...
N IV ^e	560 ⁺¹² ₋₁₁	...	3020 ⁺⁸⁷⁰ ₋₁₅₁₀	...	Ne V ^e	1050 ⁺⁸⁰ ₋₇₀	...	1050 ⁺²³⁰ ₋₂₂₀	...
O IV	3600 ⁺¹⁰⁰ ₋₉₅	...	>3600 ₋₇₂₀	>0.42 _{-0.08}	Ne VI	1900 ⁺²⁴⁰ ₋₂₀₀	...	>1900 ₋₄₂₀	>0.72 _{-0.16}
O IV ^{*i}	1790 ⁺⁷⁰ ₋₇₀	...	>1790 ₋₃₇₀	...	Ne VIII	12100 ⁺⁴⁰⁰ ₋₃₀₀	14100 ⁺²⁴⁰⁰ ₋₅₀₀	14100 ⁺³⁷⁰⁰ ₋₂₉₀₀	1.00 ^{+0.26} _{-0.21}
O IV ^e	1770 ⁺⁷⁰ ₋₇₀	...	6160 ⁺⁴⁶⁶⁰ ₋₄₃₉₀	...	Na IX	670 ⁺¹⁸⁰ ₋₂₂₀	...	<670 ⁺²⁶⁰	<1.73 ^{+0.67}
O V	940 ⁺⁵¹ ₋₄₃	...	>940 ₋₂₀₀	>0.01 _{-0.002}	Mg X	6500 ⁺²⁰⁰ ₋₁₈₀	8100 ⁺²⁰⁰ ₋₁₈₀	8100 ⁺¹⁶⁰⁰ ₋₁₆₀₀	1.02 ^{+0.20} _{-0.20}
O V ^{*j}	1000 ⁺¹⁰⁰ ₋₉₀	...	>1000 ₋₂₂₀	...	S III	26 ^{+7.8} _{-6.7}	...	<26 ^{+9.4}	<55.6 ^{+20.1}
O V ^e	940 ⁺⁵¹ ₋₄₃	...	87100 ⁺⁵⁴²⁰⁰ ₋₄₄₄₀₀	...	S IV	35 ^{+6.1} _{-5.2}	...	<35 ^{+9.3}	<4.00 ^{+1.06}
Ne VIII	7300 ⁺⁹⁶ ₋₈₈	...	>7300 ₋₁₅₀₀	>0.02 _{-0.004}	S V	18 ^{+2.0} _{-1.9}	...	>18 _{-4.0}	>0.90 _{-0.20}
Na IX	3700 ⁺¹³⁰ ₋₁₂₀	...	>3700 ₋₇₆₀	>0.98 _{-0.20}	Ar VII	3.8 ^{+2.8} _{-1.9}	...	<3.8 ^{+2.8}	<0.91 ^{+0.67}
Mg X	11000 ⁺⁸⁸⁰ ₋₆₆₀	...	>11000 ₋₂₄₀₀	>0.16 _{-0.03}	Ar VIII	30 ⁺¹⁴ ₋₁₂	...	<30 ⁺¹⁵	<5.10 ^{+2.55}
S IV	28 ^{+5.2} _{-4.9}	...	<28 ^{+7.6}	<1.00 ^{+0.29}	S3: v = -5300 km s ⁻¹				
S V	93 ^{+5.2} _{-4.8}	...	>93 ₋₁₉	>0.33 _{-0.07}	N IV	48 ^{+9.2} _{-8.5}	...	<48 ⁺¹³	<12.3 ^{+3.32}
S VI	390 ⁺¹³⁰ ₋₁₂₀	...	>390 ₋₁₄₀	>0.19 _{-0.07}	O IV	120 ⁺³¹ ₋₃₄	...	<120 ⁺⁴⁰	<6.52 ^{+2.21}
Cl VII	190 ⁺¹³ ₋₁₂	...	>190 ₋₄₀	>1.05 _{-0.22}	Ne VIII	770 ⁺⁴⁰ ₋₃₇	...	>770 ₋₁₆₀	>0.05 _{-0.01}
Ar VI	1100 ⁺⁶⁵ ₋₆₂	...	>1100 ₋₂₃₀	>0.52 _{-0.11}	Na IX	340 ⁺⁵⁹ ₋₅₄	...	>340 ₋₉₀	>1.00 _{-0.26}
Ar VIII	1100 ⁺⁴⁵ ₋₄₁	...	>1100 ₋₂₃₀	>0.30 _{-0.06}	Mg X	1500 ⁺¹²⁰ ₋₁₁₀	...	>1500 ₋₃₃₀	>0.25 _{-0.05}
K IX	210 ⁺⁵⁰ ₋₄₀	...	<210 ⁺⁶⁶	<1.00 ^{+0.31}	Si XI	96000 ⁺¹⁰⁰⁰ ₋₅₈₀₀₀	...	<96000 ⁺¹⁹⁰⁰⁰	<62.6 ^{+12.5}
Ca VI	2700 ⁺⁴⁵⁰ ₋₃₆₀	...	<2700 ⁺⁷⁰⁰	<0.98 ^{+0.25}	Ar VII	5.1 ^{+3.1} _{-2.4}	...	<5.7 ^{+3.3}	<6.74 ^{+4.36}
S2: v = -12900 km s ⁻¹					Ar VIII	32 ⁺¹⁵ ₋₁₅	...	<32 ⁺¹⁶	<11.10 ^{+6.45}
H I	9100 ⁺¹⁵⁰⁰ ₋₁₉₀₀	...	<9100 ⁺²³⁰⁰	<127 ^{+32.5}	Ca X	46 ⁺³² ₋₁₈	...	<46 ⁺³³	<1.37 ^{+0.98}
O IV	460 ⁺⁴² ₋₃₉	...	<460 ⁺¹⁰⁰	<7.30 ^{+1.60}	S4: v = -5770 km s ⁻¹				
O V	290 ⁺³³ ₋₂₈	...	>290 ₋₆₄	>0.17 _{-0.04}	N IV	240 ⁺¹³ ₋₁₁	...	>240 ₋₄₉	>0.34 _{-0.07}
Ne VIII	3400 ⁺⁵⁹ ₋₅₆	...	>3400 ₋₆₈₀	1.00 _{-0.20}	O III	75 ⁺³⁹ ₋₂₉	...	<75 ⁺⁴²	<1.04 ^{+0.58}
Na IX	220 ⁺⁵⁷ ₋₄₈	...	<220 ⁺⁷¹	<10.4 ^{+3.37}	O IV	660 ⁺⁵⁹ ₋₅₃	...	>660 ₋₁₄₀	>0.13 _{-0.03}
Mg X	2200 ⁺⁶³⁰ ₋₃₅₀	...	<2200 ⁺⁶⁸⁰	<6.61 ^{+2.07}	O V	570 ⁺²⁴ ₋₂₀	...	>570 ₋₁₂₀	>0.02 _{-0.004}
S V	34 ^{+2.9} _{-2.7}	...	<34 ^{+7.5}	<55.8 ^{+12.1}	Ne V ^{*g}	250 ⁺⁸⁰ ₋₅₀	...	250 ⁺⁹⁰ ₋₇₀	...
S VI	110 ⁺¹⁸ ₋₁₈	...	<110 ⁺²⁹	<29.0 ^{+7.44}	Ne V ^e	3550 ⁺⁷⁴⁰⁰ ₋₂₆₈₀	...
7C 1631+3930					Ne VIII	6000 ⁺¹⁹⁰ ₋₁₆₀	...	>6000 ₋₁₂₀₀	>0.13 _{-0.03}
S1: v = -1010 km s ⁻¹					Na IX	600 ⁺⁸⁴ ₋₇₇	...	>600 ₋₁₄₀	>1.53 _{-0.36}
O IV	170 ⁺⁴⁰ ₋₄₀	...	<170 ⁺⁵⁰	<29.6 ^{+8.71}	Mg X	3400 ⁺¹⁷⁰ ₋₁₅₀	4300 ⁺²⁷⁰ ₋₂₁₀	4300 ⁺⁹⁰⁰ ₋₈₉₀	0.81 ^{+0.17} _{-0.17}
O V	310 ⁺¹⁰ ₋₁₀	...	>310 ₋₆₀	>1.01 _{-0.20}	S IV	28 ^{+5.3} _{-3.5}	...	<28 ^{+7.8}	<2.59 ^{+0.71}
Ne V	350 ⁺⁷⁰ ₋₇₀	...	<350 ⁺¹⁰⁰	<9.08 ^{+2.60}	S V	28 ^{+3.4} _{-3.2}	...	>28 _{-6.4}	>0.74 _{-0.17}
Ne VI ^{*f}	160 ⁺⁷⁰ ₋₇₀	...	<160 ⁺⁷⁰	...	Ar VII	39 ^{+4.9} _{-4.8}	...	>39 _{-9.3}	>1.02 _{-0.24}
Ne VI ^e	780 ⁺⁶⁵⁰ ₋₁₉₀	...	Ar VIII	96 ⁺²³ ₋₂₀	...	<96 ⁺³⁰	<0.95 ^{+0.30}
Ne VIII	4100 ⁺¹⁷⁰ ₋₁₄₀	5400 ⁺¹⁶⁰⁰ ₋₃₄₀	5400 ⁺²⁰⁰⁰ ₋₁₁₀₀	0.97 ^{+0.35} _{-0.20}	Ca X	540 ⁺⁷⁰ ₋₅₇	...	<540 ⁺¹³⁰	<1.45 ^{+0.35}
Mg X	2200 ⁺¹¹⁰ ₋₁₀₀	2500 ⁺¹³⁰ ₋₁₁₀	2500 ⁺⁵²⁰ ₋₅₂₀	1.01 ^{+0.21} _{-0.21}	S5: v = -6150 km s ⁻¹				
Ar VII	8.4 ^{+3.3} _{-3.3}	...	<8.4 ^{+3.7}	<34.5 ^{+15.2}	N IV	9.3 ^{+2.5} _{-4.4}	...	<9.3 ^{+3.1}	<1.80 ^{+0.60}
Ar VIII	32 ^{+9.0} ₋₁₃	...	<32 ⁺¹¹	<34.8 ^{+12.0}	O V	76 ^{+7.3} _{-7.2}	...	>76 ₋₁₇	>0.06 _{-0.01}
S2: v = -1430 km s ⁻¹					Ne VIII	2200 ⁺⁹⁸ ₋₈₈	...	>2200 ₋₄₄₀	>0.11 _{-0.02}
N IV	270 ⁺¹⁰ ₋₁₀	...	>270 ₋₅₅	>0.92 _{-0.21}	Na IX	450 ⁺⁶⁴ ₋₅₇	...	>450 ₋₁₁₀	>1.00 _{-0.24}
O III	51 ⁺¹² ₋₂₂	...	<51 ⁺¹⁶	<0.98 ^{+0.31}	Mg X	890 ⁺¹¹⁰ ₋₉₈	...	>890 ₋₂₀₀	>0.11 _{-0.03}
O IV	1200 ⁺⁵⁰ ₋₅₀	...	>1200 ₋₂₅₀	>0.51 _{-0.11}	Si XI	130000 ⁺¹⁰⁰⁰ ₋₇₀₀₀₀	...	<130000 ⁺²⁶⁰⁰⁰	<66.6 ^{+13.3}
O V	1800 ⁺²¹⁰ ₋₄₀	...	>1800 ₋₃₆₀	>0.29 _{-0.06}	Ca X	49 ⁺³¹ ₋₂₆	...	<49 ⁺³³	<1.10 ^{+0.73}
Ne V	1400 ⁺¹⁰⁰ ₋₉₀	...	>1400 ₋₃₀₀	>1.05 _{-0.23}	S6: v = -7210 km s ⁻¹				
Ne V ^{*d}	250 ⁺⁴⁰ ₋₄₀	...	250 ⁺⁷⁰ ₋₆₀	...	N IV	25 ^{+5.1} _{-4.8}	...	<25 ^{+7.0}	<126 ^{+35.2}

Table 3 continued

Table 3 continued

Table 3 (*continued*)

Ion	AOD ^a	PC ^a	Adopted ^b	$\frac{\text{Adopted}}{\text{Best Model}}$ ^c
	(10^{12}cm^{-2})	(10^{12}cm^{-2})	(10^{12}cm^{-2})	
O IV	210_{-29}^{+32}	...	$<210^{+52}$	$<240^{+59.9}$
Ne VIII	1100_{-52}^{+58}	...	$>1100_{-230}$	$>1.00_{-0.20}$
Na IX	130_{-39}^{+44}	...	$<130^{+50}$	$<3.79^{+1.49}$
Mg X	680_{-71}^{+79}	...	$>680_{-150}$	$>1.00_{-0.23}$

NOTE—

^aSum of all N_{ion} from excited and ground states for a given ion in each outflow system using the AOD and PC methods.

^bThe adopted values in blue are lower limits, in red are upper limits, and in black are measurements.

^cThe ratio of the adopted values to the column densities from the best-fit Cloudy model.

^dNe v 413 cm^{-1} energy level.

^e0 cm^{-1} energy level of the respective ion.

^fNe VI 1307 cm^{-1} energy level.

^gNe v 1111 cm^{-1} energy level.

^hN IV 67416 cm^{-1} energy level.

ⁱO IV 386 cm^{-1} energy level.

^jO v 82385 cm^{-1} energy level.

(This table is available in machine-readable form.)

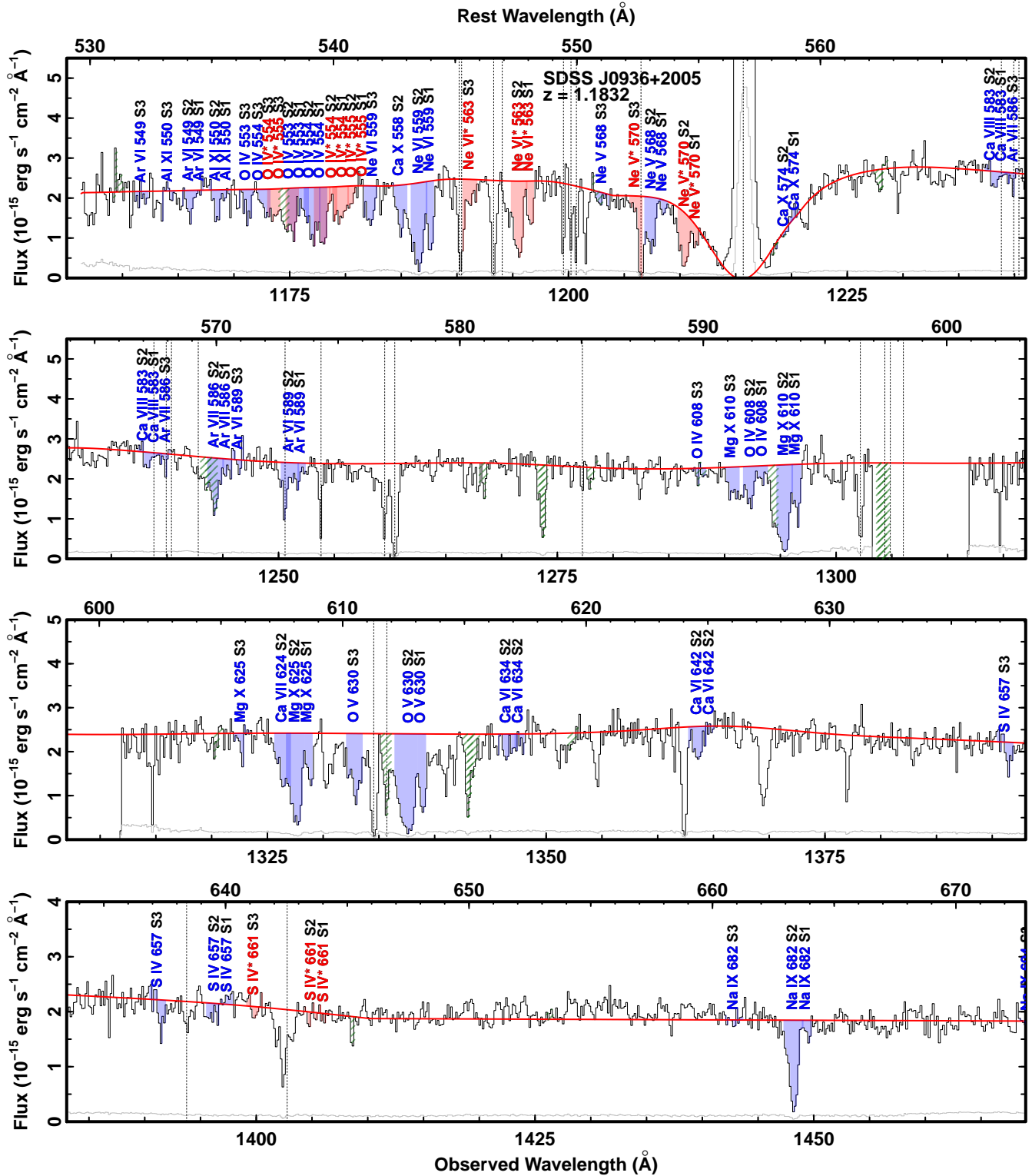


Figure 1. The dereddened HST/COS spectrum (in black) with errors (in gray) for the five quasars. The main absorption troughs are labeled for all outflow systems as well as regions used for upper limit measurements (see Table 2). Blue shaded regions mark transitions from ground absorption lines, and red shaded regions are for excited ones. Absorption troughs from intervening systems are the slanted dark green shaded regions, and the vertical dashed lines mark Galactic absorption and geocoronal emission features. The red contour traces the unabsorbed emission model for each quasar. Overlapping sections of troughs have regions of darker blues and reds as well as mixtures of blue and red.

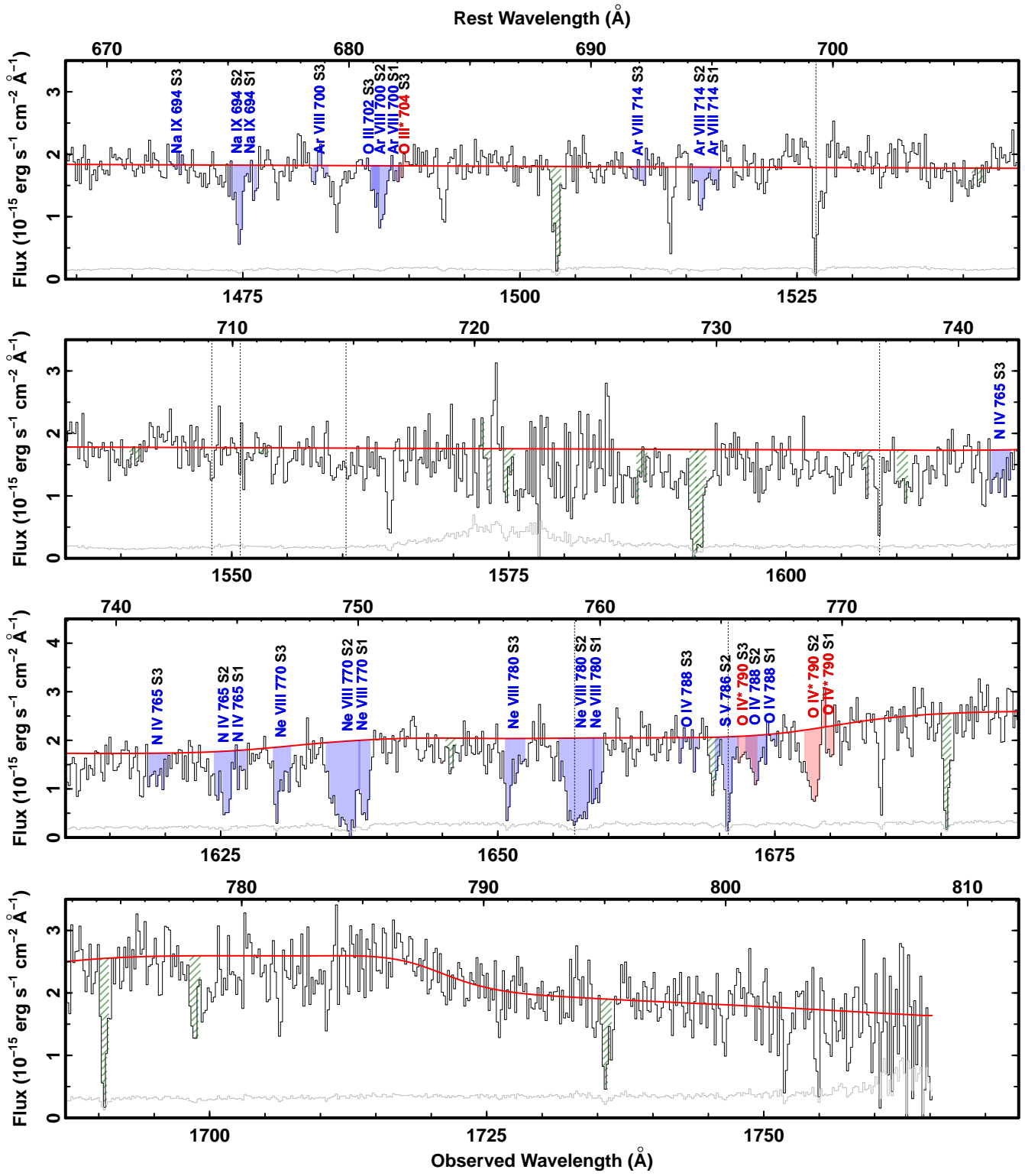


Figure 1. (Continued.)

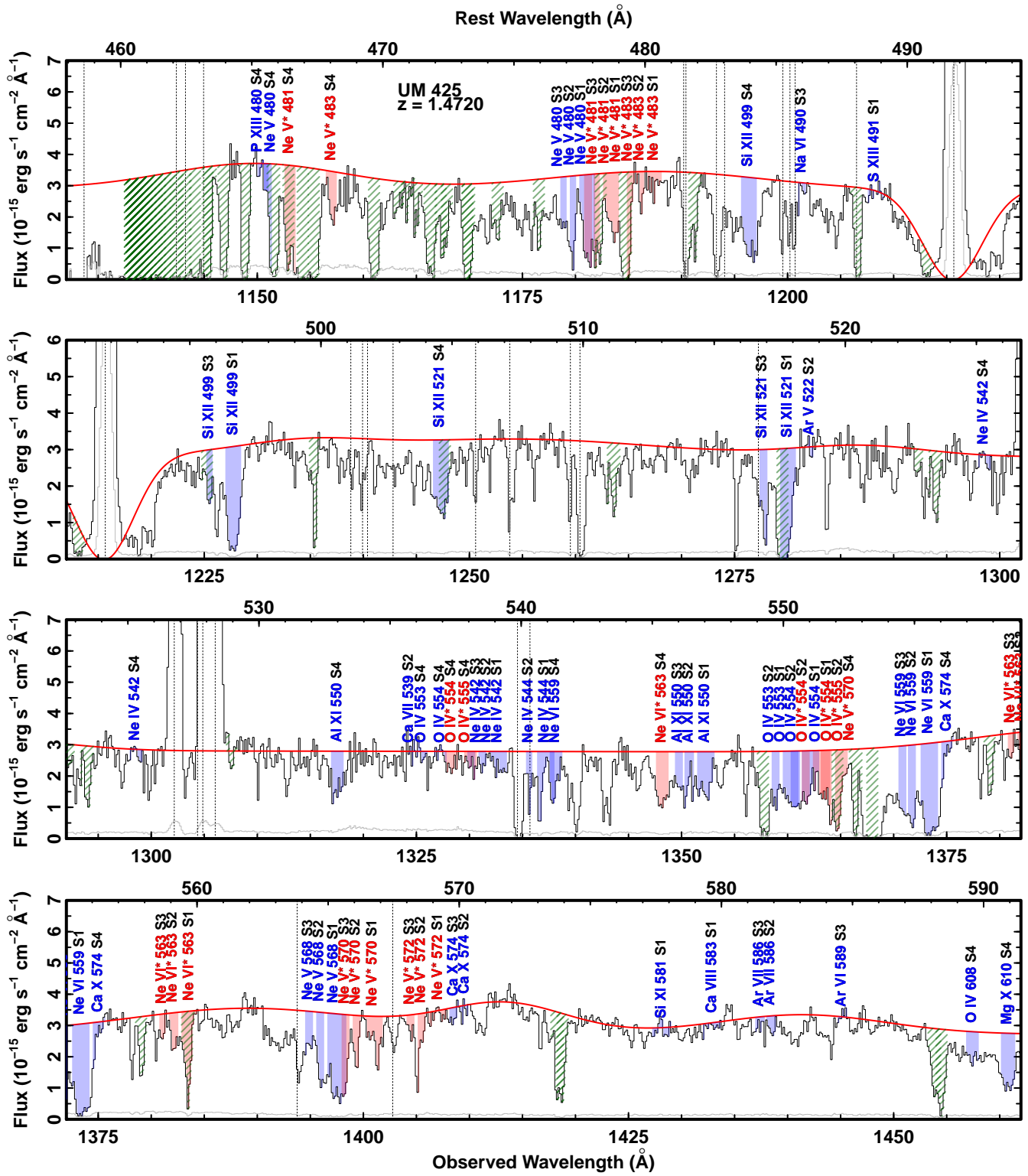


Figure 1. (Continued.)

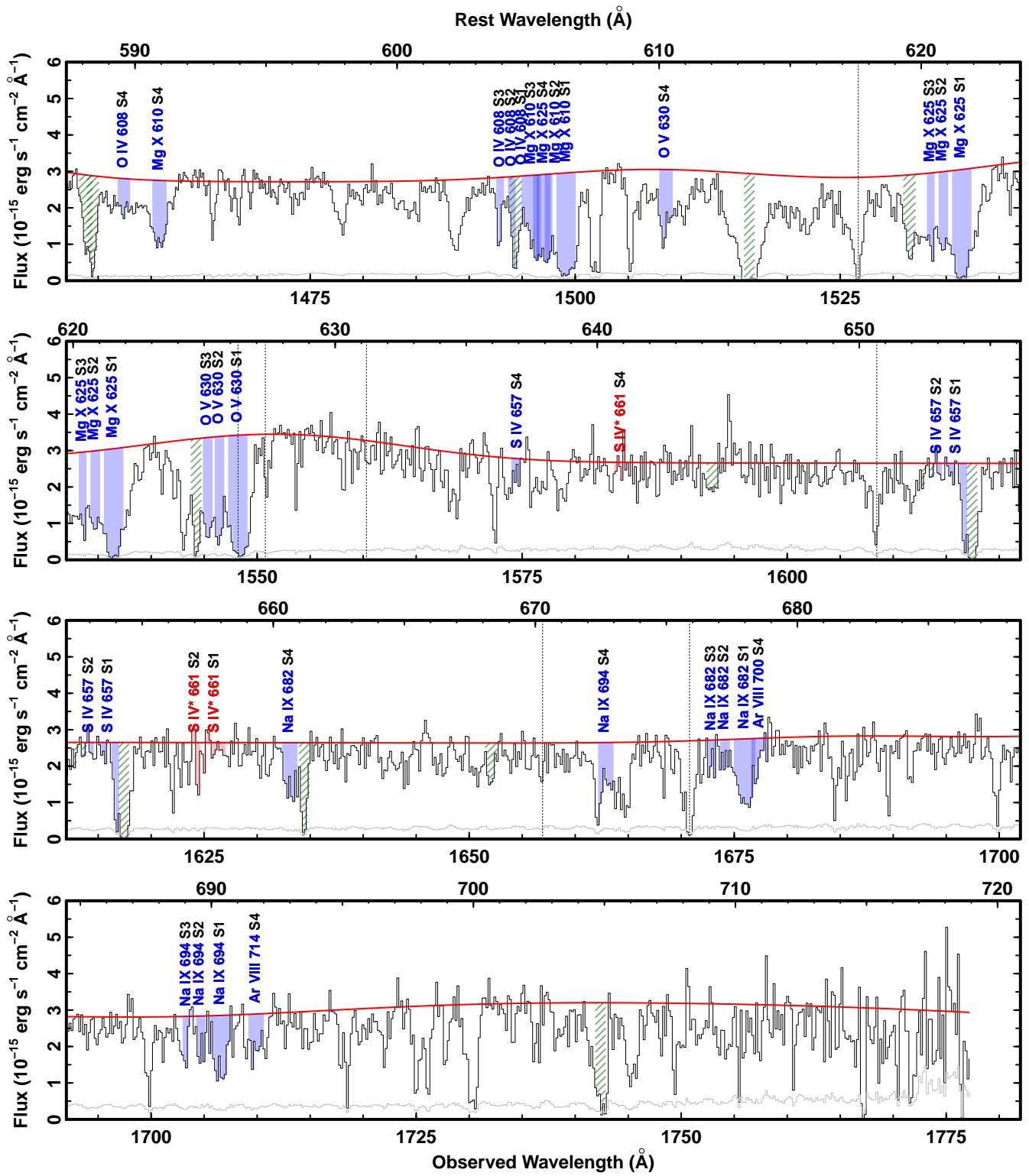
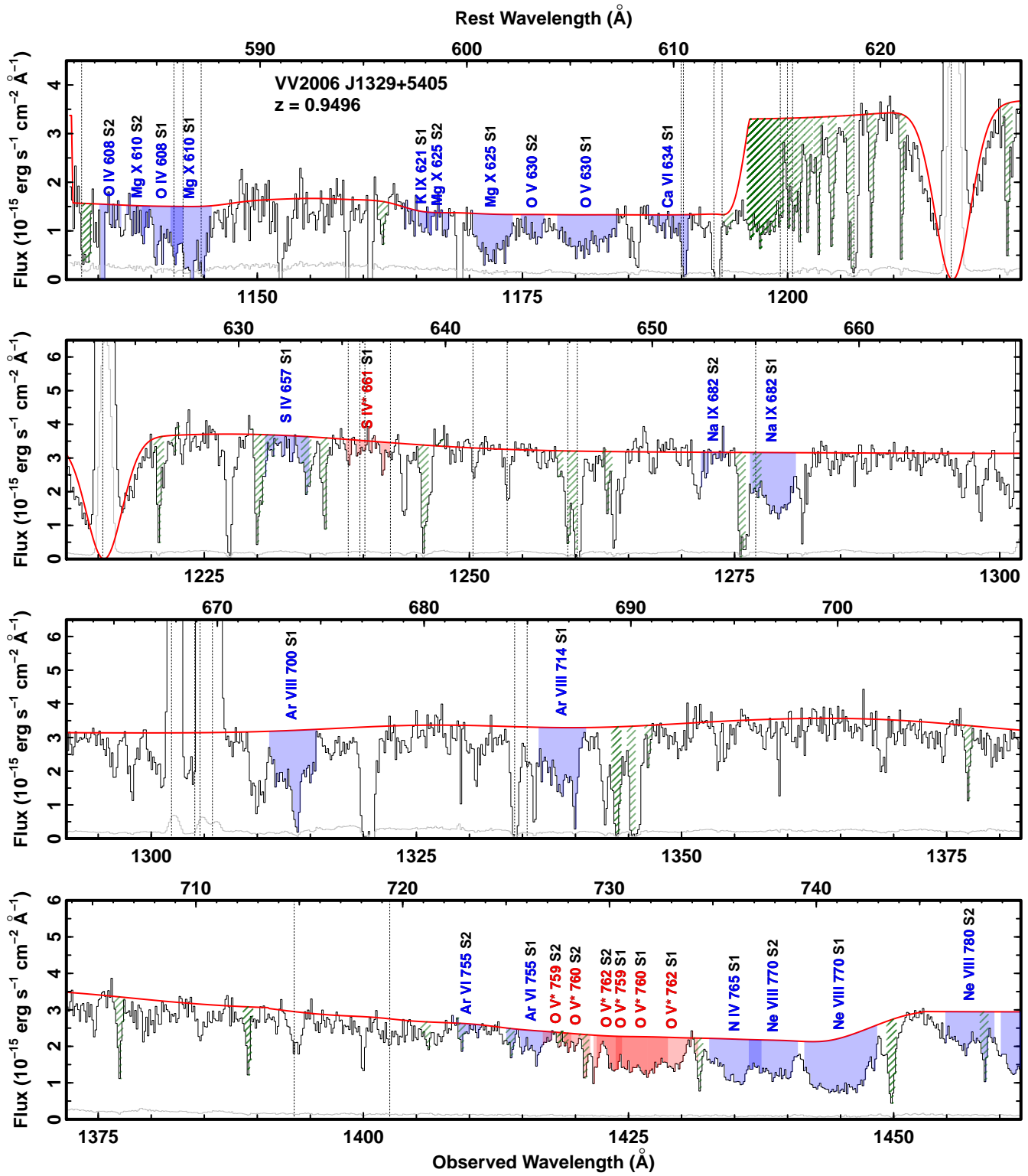


Figure 1. (Continued.)



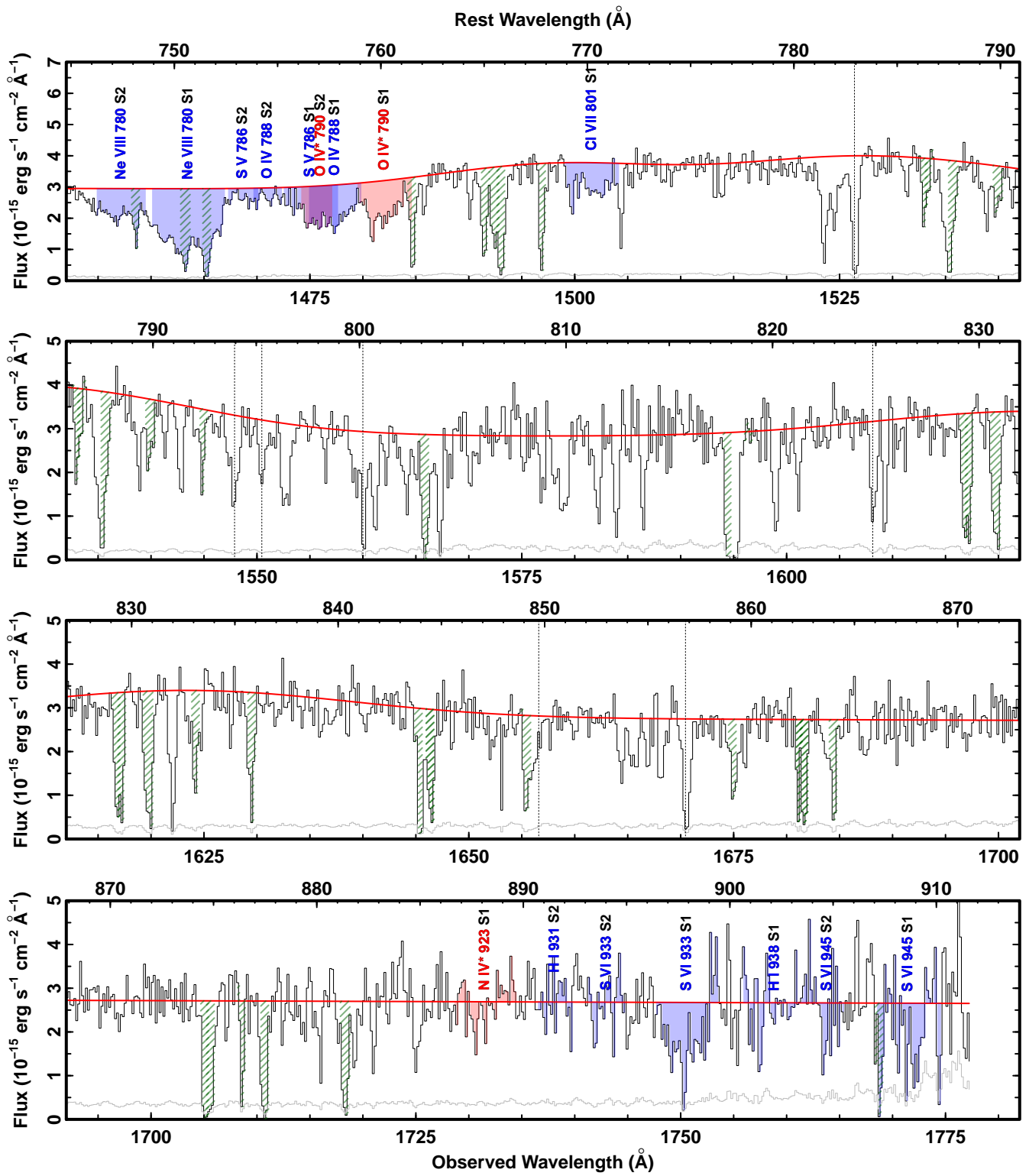


Figure 1. (Continued.)

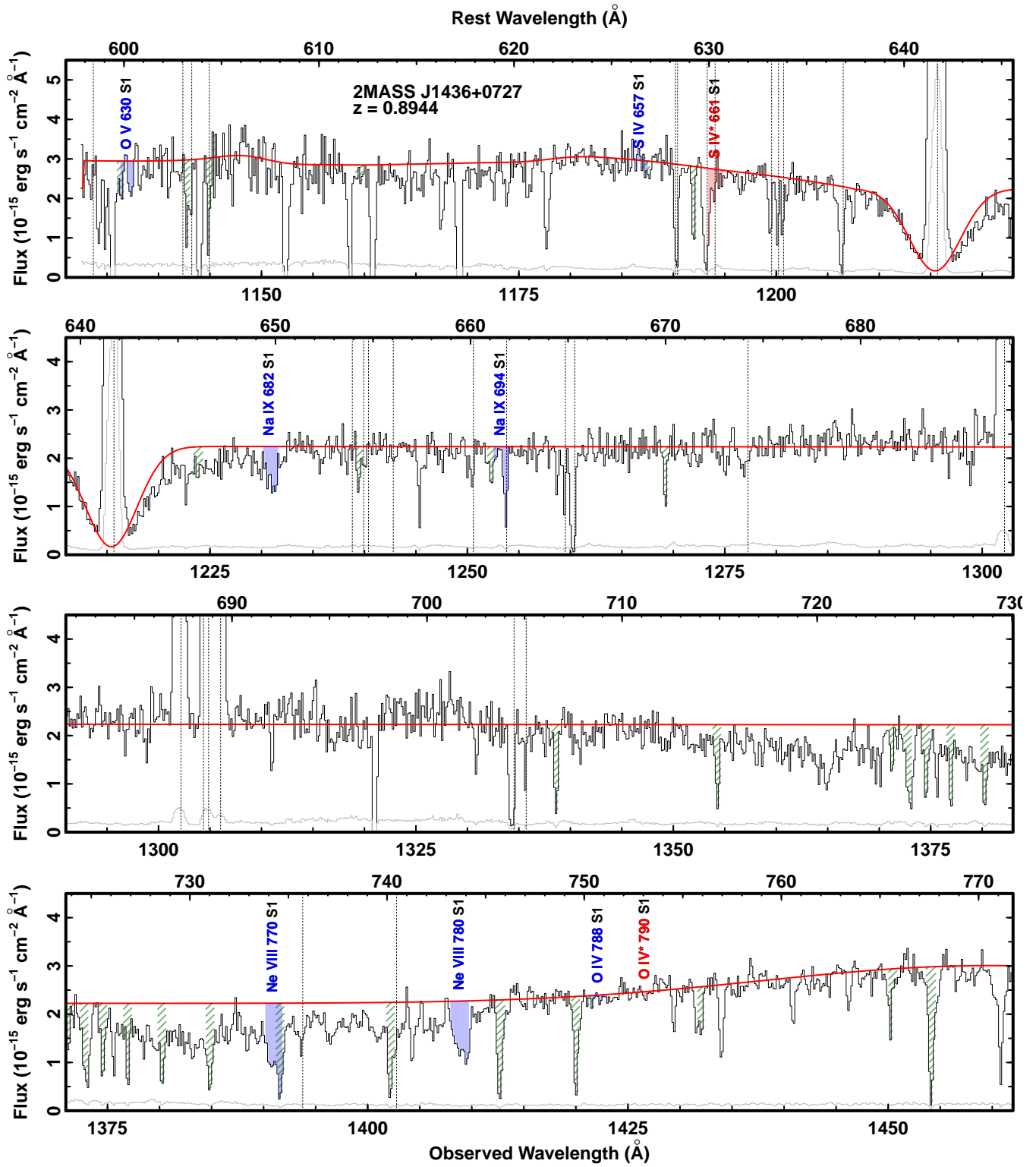


Figure 1. (Continued.)

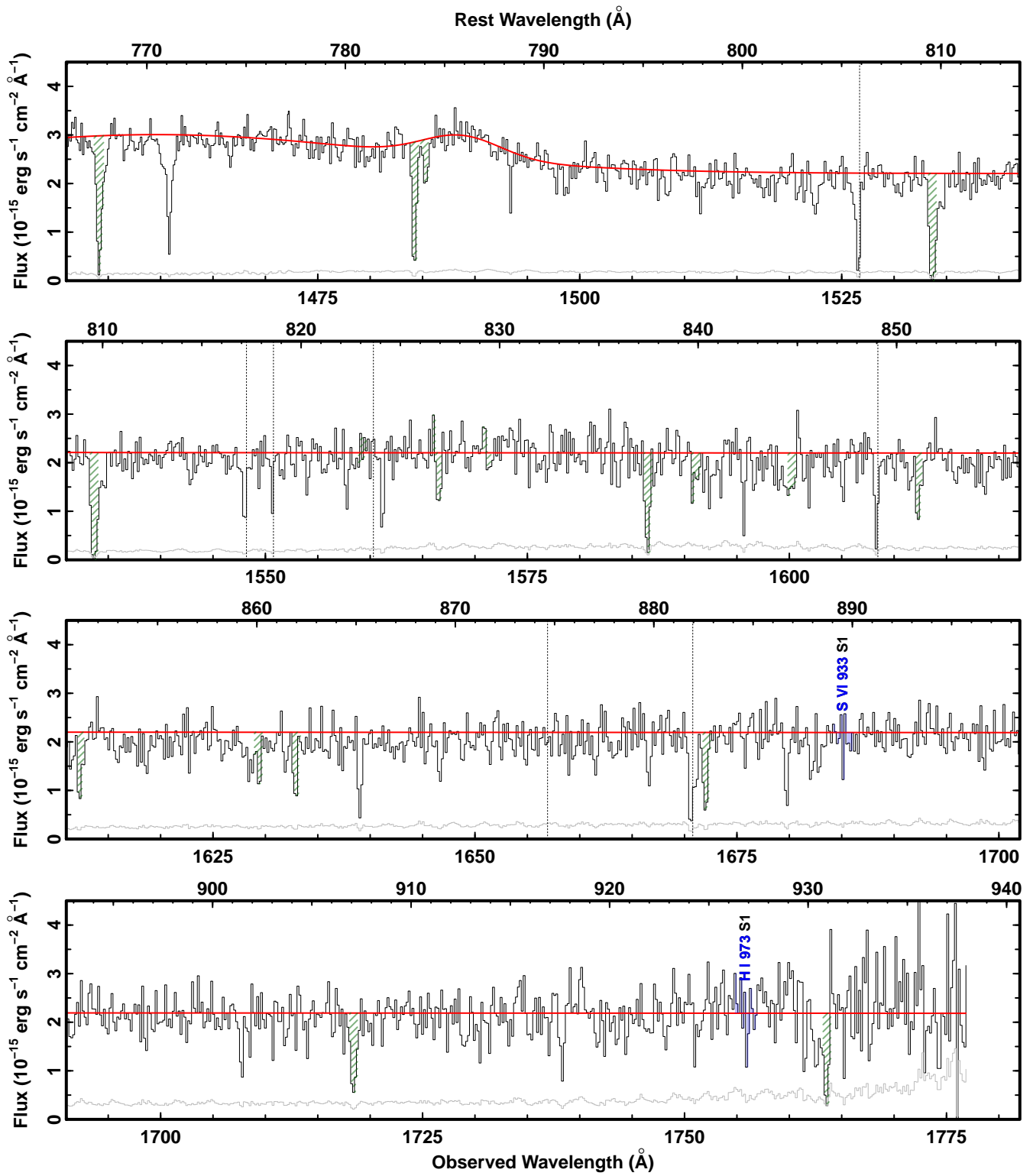


Figure 1. (Continued.)

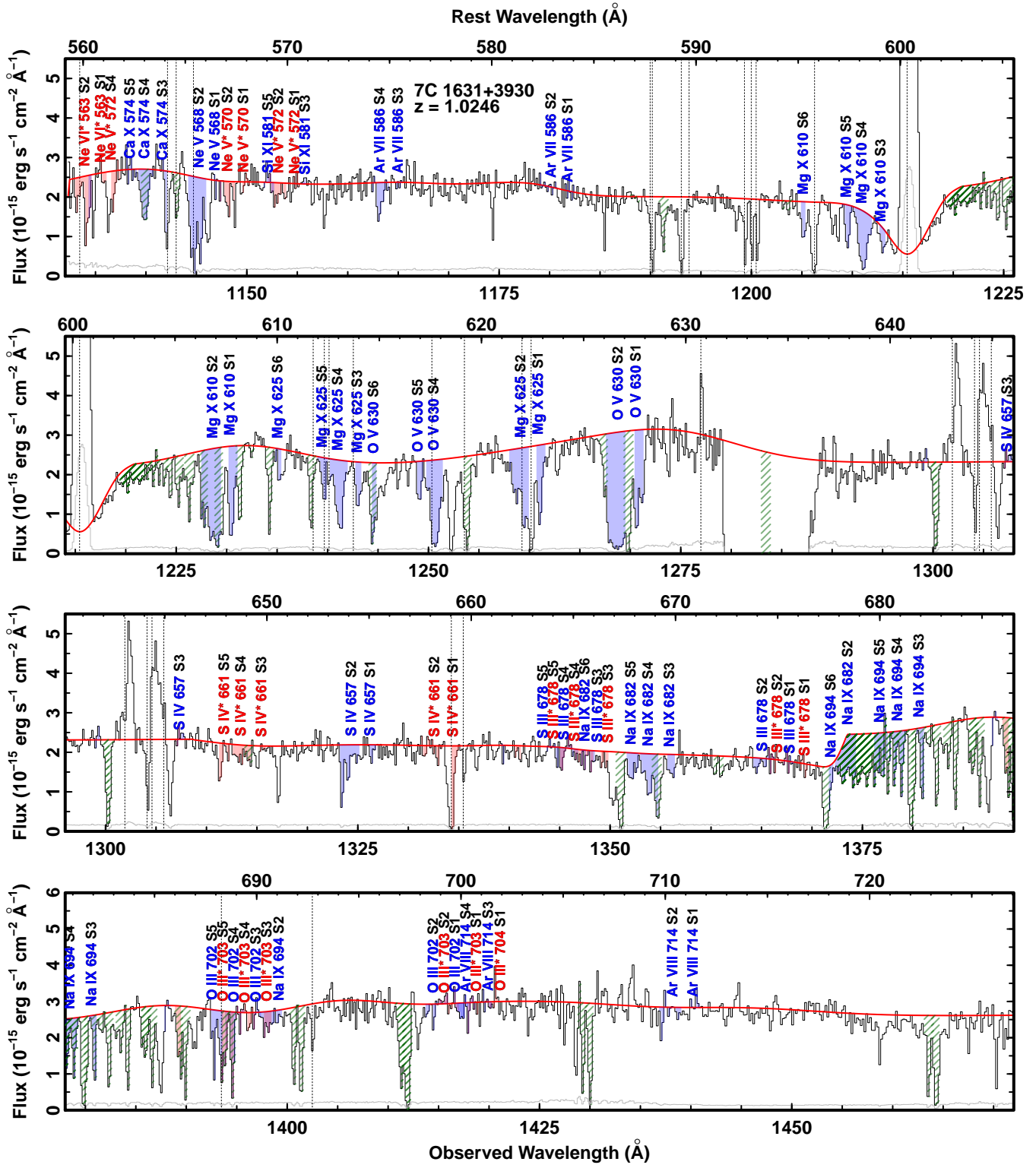


Figure 1. (Continued.)

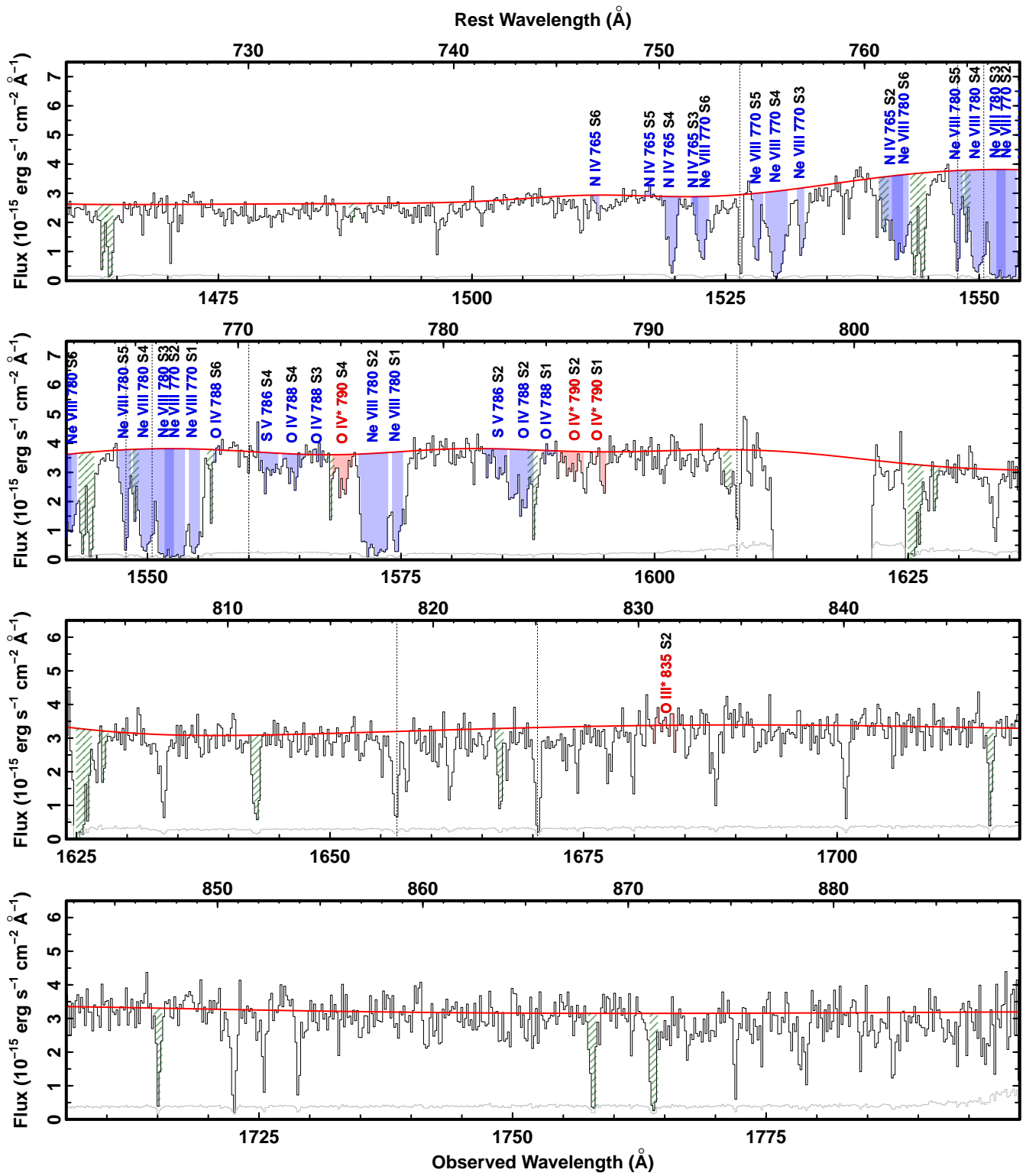


Figure 1. (Continued.)

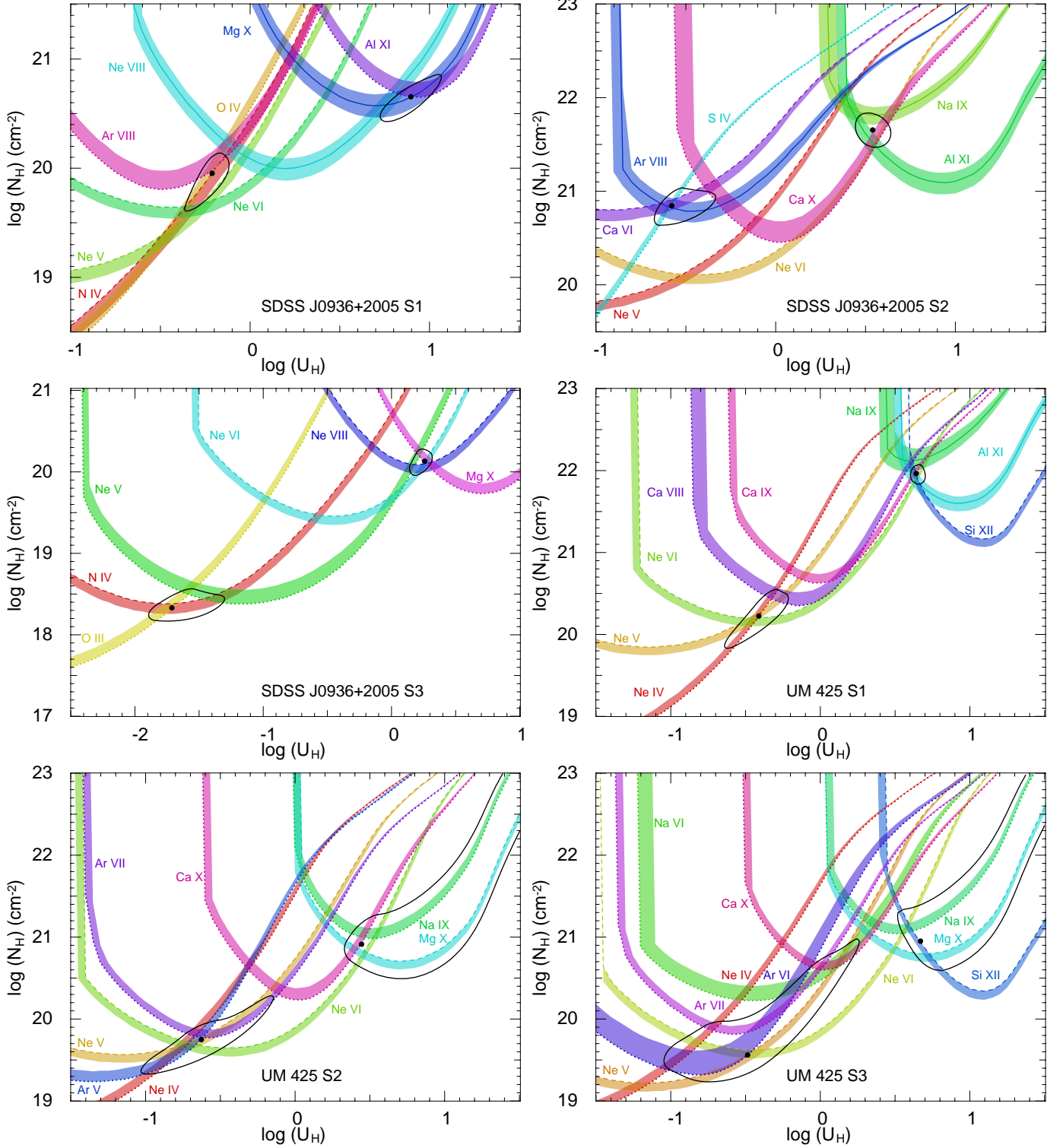


Figure 2. Photoionization solutions for each outflow system. The colored contours show the model parameters that are consistent with the observed values assuming the HE0238 SED and solar metallicity (for VV2006 J1329+5405, $Z = 4.68 Z_{\odot}$; see Table 3 of Paper V). Solid contours represent ionic column densities taken as measurements while dotted and dashed contours are upper and lower limits, respectively. The shaded bands are the 1σ uncertainties for each contour (see Table 3). The dots are the best χ^2 -minimization solutions for each ionization phase and the ellipses encircling them are their 1σ uncertainties.

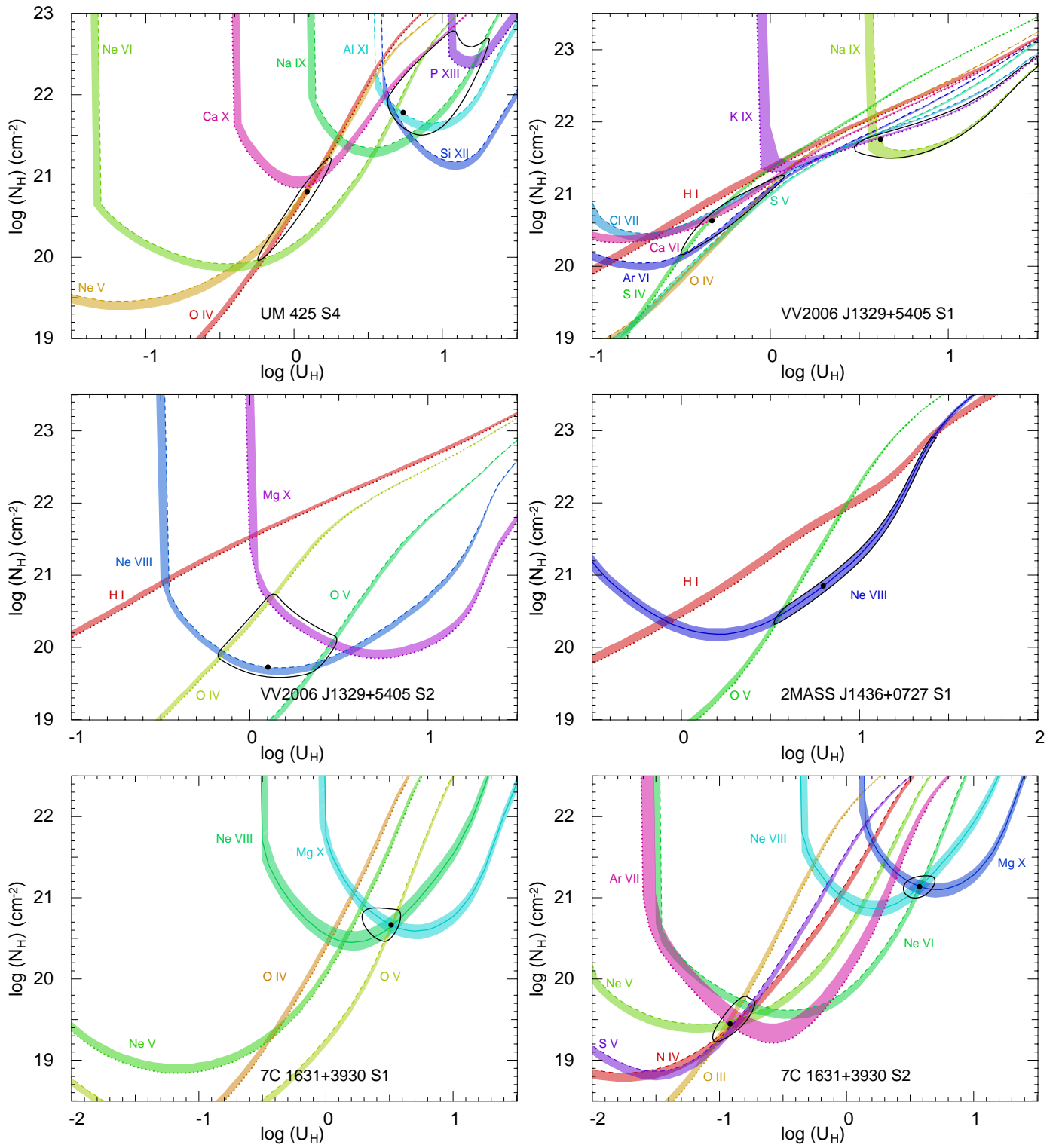


Figure 2. (Continued.)

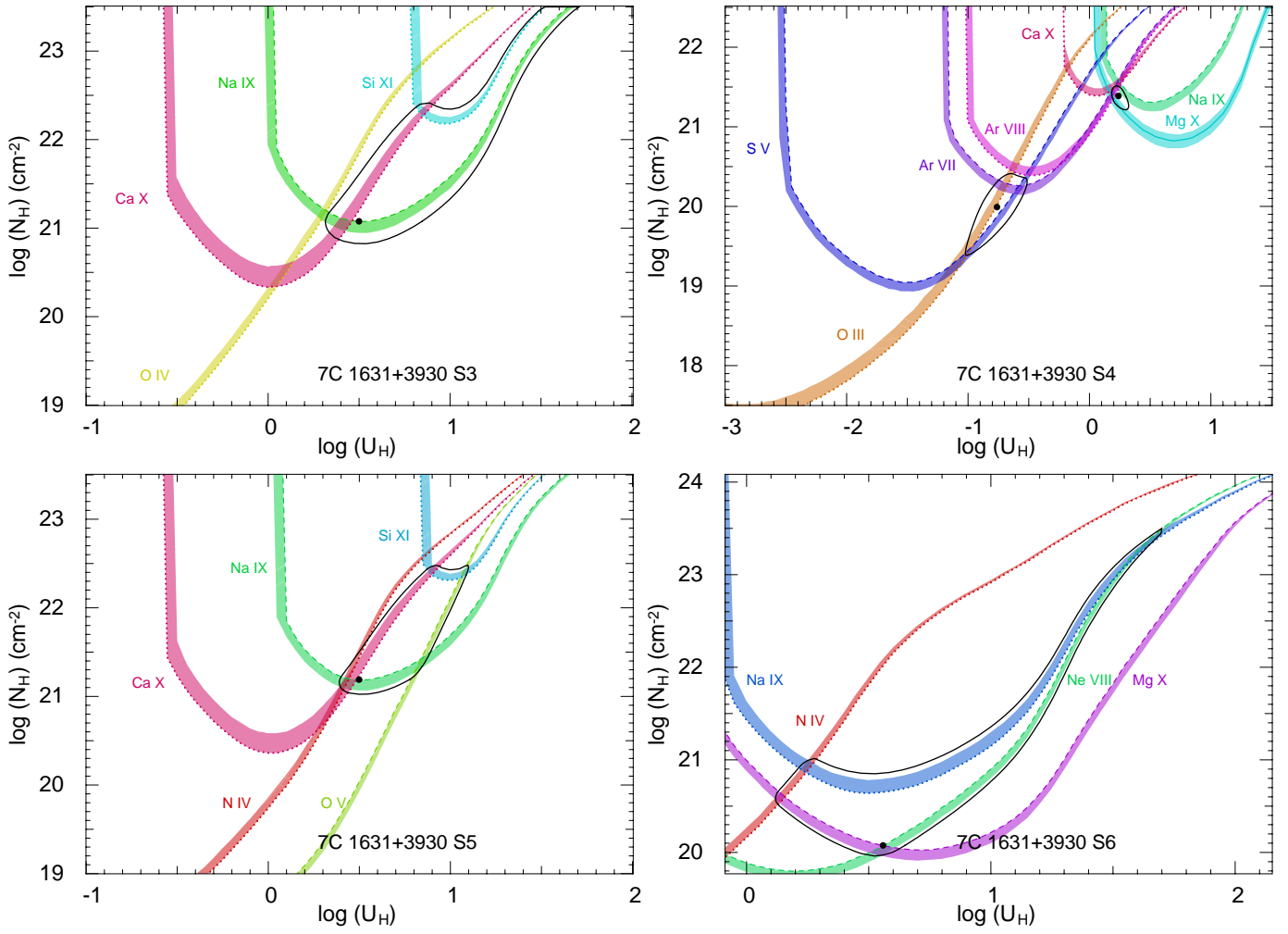


Figure 2. (Continued.)

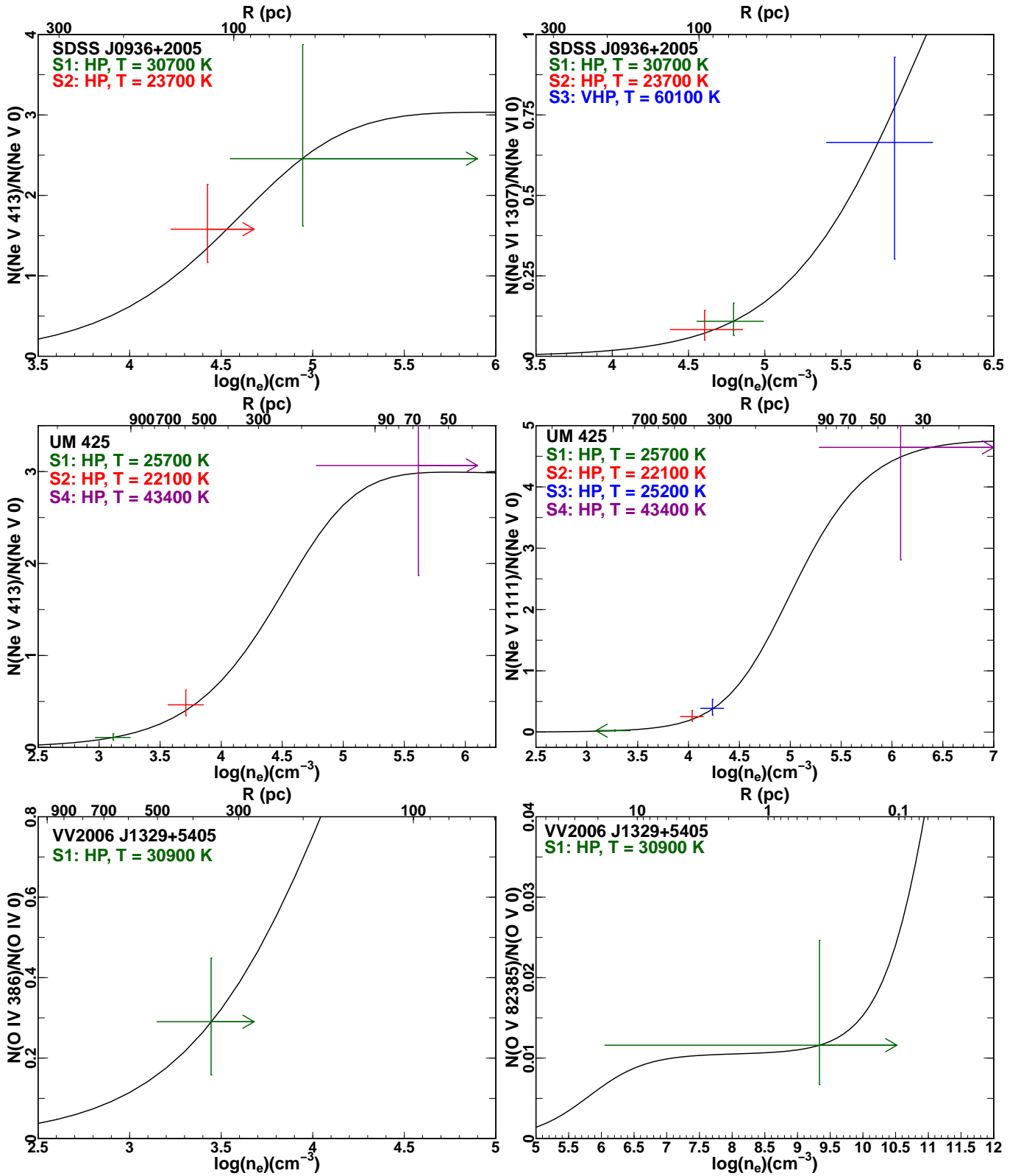


Figure 3. Electron number density, n_e , of each outflow system based on three population ratios of Ne and one of O. The theoretical predictions from CHIANTI for the population ratios with excited energy levels of Ne v* 413 cm^{-1} , Ne v* 1111 cm^{-1} , Ne VI* 1307 cm^{-1} , O IV* 386 cm^{-1} , O v* 82385 cm^{-1} , or N IV* 67416 cm^{-1} are overlaid. The curves assume the average electron temperature (T) from the photoionization solution for the corresponding phase of the first listed outflow. The distance, R (from equation 1), for the first labeled outflow is also shown on the top axis. The offset of the ratios from the shown curves for the other outflows are the result of the different temperatures.

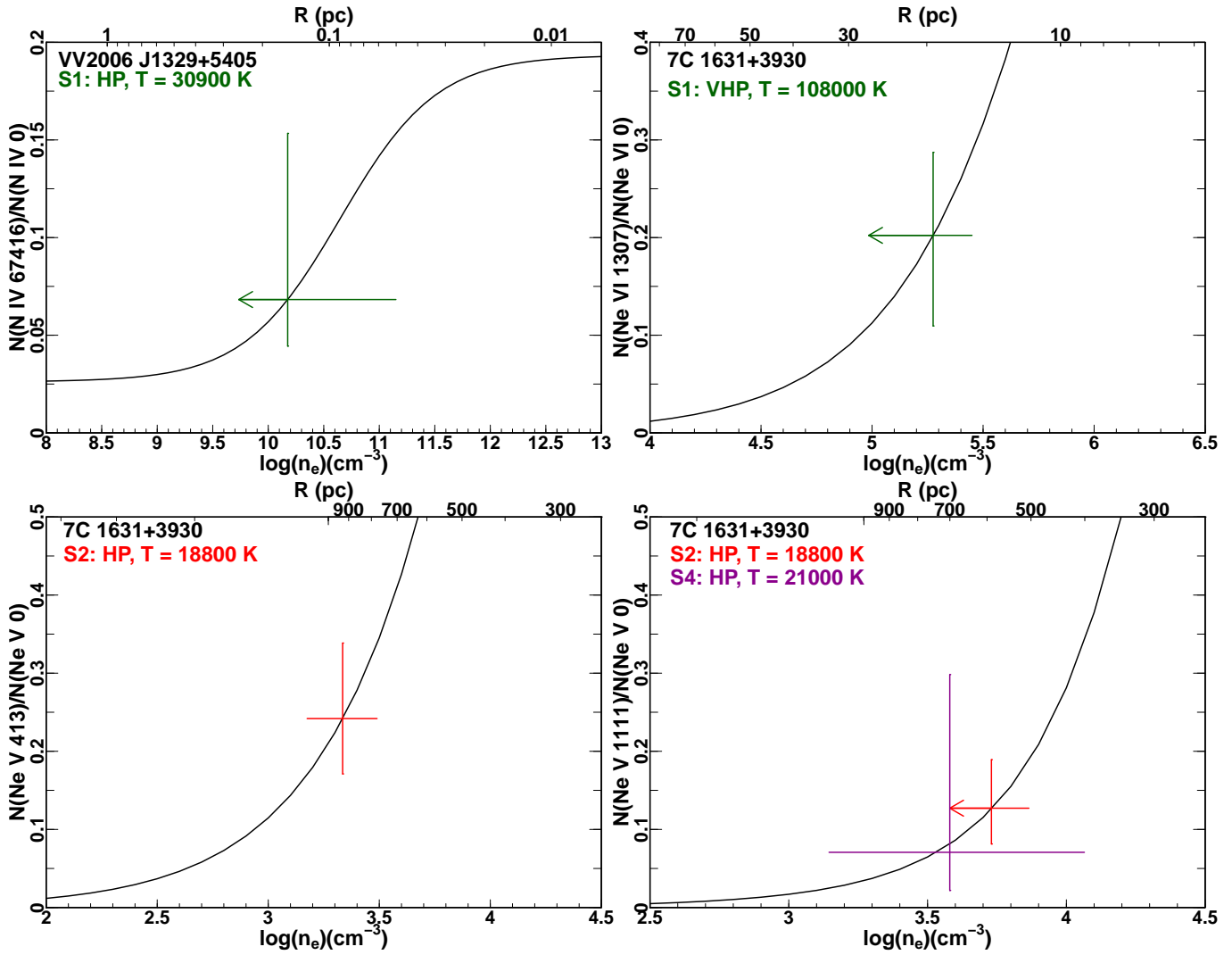


Figure 3. (Continued.)

Table 4. Physical Properties, Distances, and Energetics of Each Outflow system

System	$v^{(a)}$ (km s ⁻¹)	$\log(U_{\text{H,HP}})$	$\log(N_{\text{H,HP}})$	$\log(n_e)$	$\log(U_{\text{H,VHP}})$	$\log(N_{\text{H,VHP}})$	$\log(f_{\nu}^{(b)})$	R	$\dot{M}^{(c)}$ (M_{\odot} yr ⁻¹)	$\log \dot{E}_K^{(c)}$ log(erg s ⁻¹)	$\dot{E}_K / L_{\text{Edd}}^{(c)}$ %
SDSS J0936+2005, $L_{\text{bol}} = 1.3 \times 10^{47}$ erg s⁻¹, $L_{\text{Edd}} = 1.4_{-0.7}^{+1.5} \times 10^{47}$ erg s⁻¹, $Q_{\text{H}} = 7.2 \times 10^{56}$ s⁻¹											
1	-7960	-0.2 ^{+0.2} _{-0.3}	20.0 ^{+0.4} _{-0.6}	4.8 ^{+0.2} _{-0.2}	0.8 ^{+0.3} _{-0.3}	20.6 ^{+0.4} _{-0.3}	-1.8 ^{+0.6} _{-0.9}	77 ⁺⁴⁰ ₋₂₂	17 ⁺²⁹ _{-8.5}	44.5 ^{+0.4} _{-0.3}	0.23 ^{+0.59} _{-0.15}
2	-8200	-0.6 ^{+0.3} _{-0.1}	20.8 ^{+0.2} _{-0.2}	4.6 ^{+0.3} _{-0.2}	0.5 ^{+0.1} _{-0.1}	21.7 ^{+0.1} _{-0.2}	-1.9 ^{+0.3} _{-0.4}	150 ⁺⁵⁰ ₋₅₀	370 ⁺²⁸⁰ ₋₁₈₀	45.9 ^{+0.2} _{-0.3}	5.5 ^{+8.5} _{-3.5}
3	-9300	-1.7 ^{+0.4} _{-0.2}	18.3 ^{+0.2} _{-0.1}	5.9 ^{+0.2} _{-0.5}	0.3 ^{+0.02} _{-0.2}	20.1 ^{+0.2} _{-0.1}	-3.8 ^{+0.3} _{-0.5}	14 ⁺⁹ ₋₄	1 ⁺¹ _{-0.5}	43.4 ^{+0.3} _{-0.3}	0.01 ^{+0.3} _{-0.005}
UM 425, $L_{\text{bol}} = 3.8 \times 10^{47}$ erg s⁻¹, $L_{\text{Edd}} = 6.0_{-3.2}^{+6.3} \times 10^{47}$ erg s⁻¹, $Q_{\text{H}} = 2.1 \times 10^{57}$ s⁻¹											
1	-1640	-0.4 ^{+0.2} _{-0.2}	20.2 ^{+0.3} _{-0.4}	3.1 ^{+0.2} _{-0.1}	0.64 ^{+0.06} _{-0.04}	22.0 ^{+0.1} _{-0.2}	-2.8 ^{+0.4} _{-0.5}	1180 ⁺⁴³⁰ ₋₂₉₀	1050 ⁺⁶⁸⁰ ₋₄₇₀	44.9 ^{+0.3} _{-0.2}	0.1 ^{+0.3} _{-0.03}
2	-1980	-0.6 ^{+0.4} _{-0.4}	19.8 ^{+0.5} _{-0.4}	3.7 ^{+0.2} _{-0.1}	>0.5 _{-0.2}	>20.9 _{-0.4}	<-2.3 ^{+0.8} _{-0.8}	760 ⁺⁴⁴⁰ ₋₃₂₀	>81 ₋₅₅	>44.0 _{-0.5}	>0.02 _{-0.01}
3	-2200	-0.4 ^{+0.7} _{-0.6}	19.6 ^{+1.4} _{-0.4}	4.2 ^{+0.1} _{-0.1}	>0.7 _{-0.2}	>21.0 _{-0.4}	<-2.5 ^{+1.6} _{-1.6}	340 ⁺³⁷⁰ ₋₁₉₀	>43 ₋₃₁	>43.8 _{-0.5}	>0.011 _{-0.007}
4	-9420	0.1 ^{+0.2} _{-0.3}	20.8 ^{+0.4} _{-0.8}	>6.1 _{-0.8}	0.7 ^{+0.6} _{-0.1}	21.8 ^{+1.0} _{-0.3}	-1.6 ^{+0.5} _{-1.5}	<22 ⁺³⁷ ₋	<81 ⁺⁸⁵⁰ ₋	<45.4 ^{+1.0} ₋	<0.4 ^{+4.4} ₋
VV2006 J1329+5405, $L_{\text{bol}} = 8.9 \times 10^{46}$ erg s⁻¹, $L_{\text{Edd}} = 1.2_{-0.7}^{+1.5} \times 10^{47}$ erg s⁻¹, $Q_{\text{H}} = 5.0 \times 10^{56}$ s⁻¹											
1	-11600	-0.3 ^{+0.4} _{-0.1}	20.6 ^{+0.7} _{-0.4}	9.3 ^{+1.0} _{-3.2}	>0.6 _{-0.1}	>21.8 _{-0.3}	<-2.1 ^{+0.7} _{-0.4}	0.15 ^{+0.11} _{-0.11}	>0.6 _{-0.4}	>43.4 _{-0.6}	>0.022 _{-0.017}
2	-12900	-	-	-	0.1 ^{+0.4} _{-0.3}	19.7 ^{+1.0} _{-0.1}	-	-	-	-	-
2MASS J1436+0727, $L_{\text{bol}} = 8.3 \times 10^{46}$ erg s⁻¹, $L_{\text{Edd}} = 8.5_{-4.5}^{+8.8} \times 10^{46}$ erg s⁻¹, $Q_{\text{H}} = 4.7 \times 10^{56}$ s⁻¹											
1	-14400	-	-	-	0.8 ^{+0.6} _{-0.3}	20.9 ^{+2.0} _{-0.6}	-	-	-	-	-
7C 1631+3930, $L_{\text{bol}} = 1.2 \times 10^{47}$ erg s⁻¹, $L_{\text{Edd}} = 2.3_{-1.4}^{+2.6} \times 10^{47}$ erg s⁻¹, $Q_{\text{H}} = 6.9 \times 10^{56}$ s⁻¹											
1	-1010	-	-	<5.3 ^{+0.2} ₋	0.5 ^{+0.1} _{-0.2}	20.7 ^{+0.2} _{-0.2}	-	>19 ₋₄	>0.5 _{-0.3}	>41.2 _{-0.3}	>0.00007 _{-0.00004}
2	-1430	-0.9 ^{+0.2} _{-0.1}	19.4 ^{+0.3} _{-0.2}	3.3 ^{+0.2} _{-0.1}	0.6 ^{+0.1} _{-0.2}	21.1 ^{+0.2} _{-0.1}	-3.2 ^{+0.4} _{-0.3}	940 ⁺²⁶⁰ ₋₂₃₀	110 ⁺⁷⁰ ₋₅₀	43.8 ^{+0.3} _{-0.2}	0.03 ^{+0.05} _{-0.02}
3	-5300	-	-	-	>0.5 _{-0.2}	>21.1 _{-0.3}	-	-	-	-	-
4	-5770	-0.8 ^{+0.3} _{-0.2}	20.0 ^{+0.4} _{-0.6}	3.6 ^{+0.5} _{-0.5}	0.2 ^{+0.1} _{-0.02}	21.4 ^{+0.1} _{-0.2}	-2.4 ^{+0.7} _{-0.5}	590 ⁺⁴⁷⁰ ₋₂₇₀	500 ⁺⁵²⁰ ₋₂₉₀	45.7 ^{+0.3} _{-0.4}	2.3 ^{+4.9} _{-1.4}
5	-6150	-	-	-	0.5 ^{+0.6} _{-0.1}	21.2 ^{+1.3} _{-0.2}	-	-	-	-	-
6	-7210	-	-	-	0.6 ^{+1.1} _{-0.5}	20.1 ^{+3.4} _{-0.1}	-	-	-	-	-

NOTE—

(a). The velocity centroid of each outflow system.

(b). The volume filling factor of the outflow's high-ionization phase relative to the very high-ionization phase.

(c). Assuming $\Omega = 0.4$ and where N_{H} is the sum of the two ionization phases, if present.

6. DISCUSSION

6.1. Contribution to AGN Feedback

The potential for AGN feedback can be assessed by using the criterion set forth by Hopkins & Elvis (2010) or Scannapieco & Oh (2004) where the kinetic luminosities must exceed 0.5% or 5% of the Eddington luminosity (L_{Edd}), respectively. We use the Mg II-based black hole mass equation from Bahk et al. (2019) along with their methodology for measuring the Mg II FWHM and the nearby continuum level from Sloan Digital Sky Survey (SDSS) data to estimate the mass of the super massive black hole, which is then used to calculate L_{Edd} (see Table 4; errors include systematics). Outflow S4 in 7C 1631+3930 has a kinetic luminosity above 0.5% L_{Edd} while outflow S2 in SDSS J0936+2005 exceeds 5% L_{Edd} . Therefore, on average, these two outflows carry enough energy, depending on the method of energy deposition into the surrounding ISM of the host galaxy, to contribute substantially to AGN feedback in galaxies with similar black hole masses as each of these quasars.

6.2. Photoionization Solution and n_e Accuracy

The majority of the photoionization solutions shown in Figure 2 are constrained only by N_{ion} upper and lower limits. As such, they are immune to saturation effects. Measurements were only taken for doublet transitions where a partial covering solution could be reliably determined or for single transitions where we could infer that saturation effects would be minimal. The multitude of upper and lower limits along with the few measurements yielded only four out of the 16 outflows with unbounded VHPs. Half of the bounded VHPs have tightly constrained errors to within a factor of two. The photoionization solutions of either the HP (two phase solutions) or VHP (single phase solutions) constrained the total N_{ion} for Ne v, Ne VI, O IV, O v, and N IV, which were used in conjunction with the excited- and ground-state N_{ion} measured from the data to calculate the population ratios that yielded n_e for each outflow (see sections 3.3 and 4). When multiple diagnostics were available for a given outflow, the n_e values were all consistent within errors. This consistency in n_e between multiple diagnostics that arose from constraints from the photoionization solutions shows the results are robust and reliable.

6.3. Geometry and Volume Filling Factor

Comparing outflows within a given quasar, there are two that show a similarity in their respective geometries: S1 and S2 in SDSS J0936+2005. The kinematic similarities of the troughs from the VHP and HP for each outflow suggest that the two phases occupy the same volume. Under the assumption that the VHP occupies the total volume where the outflow resides (i.e., the volume filling factor = 1; Arav et al. 2013), and since the HP is both denser and has a lower N_{H} than that of the

VHP, the HP would have a small volume filling factor within the VHP. This volume filling factor is given by equation 4 in Section 3.5 of Paper I:

$$f_v = \frac{U_{\text{H,HP}}}{U_{\text{H,VHP}}} \times \frac{N_{\text{H,HP}}}{N_{\text{H,VHP}}} \quad (4)$$

S1 and S2 in SDSS J0936+2005 have f_v values that are fully consistent, considering the errors (see Table 4). This similarity in geometry, the consistent distances, and small velocity separation (240 km s⁻¹) suggest the two outflows have a common origin. These similarities in geometry, distance, and velocity were also observed for outflows 1a and 1b in Paper II as well as the four outflows in Paper III, implying that it is more than a coincidence.

6.4. Comparison to X-Ray Warm Absorbers

As has been discussed in Papers II, III, and V, X-ray warm absorbers span a wide range of U_{H} , which can be explained by a continuous N_{H} absorber as a function of U_{H} . The single phase and two phase solutions found here are sufficient to explain the data, but we cannot rule out additional ionization phases that are not detected due to the wavelength range and/or data sensitivity limitations. Also, the U_{H} values in Table 4 are comparable to the quantity $\log(\xi)$ that is commonly used in X-ray analyses [$\log(\xi) \approx \log(U_{\text{H}})+1.3$]. Therefore, the outflows detected here are similar to X-ray warm absorbers.

6.5. New Absorption Trough Transitions/Ions

To the best of our knowledge, the detection of Cl VII 800.64 Å in S1 of VV2006 J1329+5405 is a first in both ion and transition for the astronomical community. Similarly, the Ne v 480.42 Å and Ne v* 482.99 Å line transitions in S4 of UM 425 are also first time detections.

7. SUMMARY AND CONCLUSIONS

This paper presented new HST/COS spectra for five quasars containing 16 outflows. Absorption troughs from up to 14 ions yielded column density measurements and lower limits for each outflow. The use of these absorption trough constraints along with additional upper limits and a grid of photoionization models enabled us to determine the best-fitting values of U_{H} and N_{H} for each outflow.

Column density ratios from excited- and ground-state transitions of Ne v, Ne VI, O IV, O v, and N IV constrained the electron number densities of 11 outflows. Using those values, the distances of each outflow to the central source were calculated from equation (1), leading to the mass flux and kinetic luminosity (equations 2 and 3). Lastly, the potential for AGN feedback was investigated with the final results summarized in Table 4.

The main results are as follows:

1. Of the 16 outflows, 10 require a two phase photoionization solution to simultaneously satisfy the

- column density measurements from ions spanning over an order of magnitude in ionization potential. Each of the other six contain a VHP.
2. Distances and energetics were determined for 11 outflows with seven having more than one distance indicator, and all of these were consistent within errors. Outflows S2 in SDSS J0936+2005 and S4 in 7C 1631+3930 each have a large enough kinetic luminosity to Eddington luminosity ratio to be major contributors to AGN feedback processes, depending on the energy deposition process. If the electron number density of outflow S1 in VV2006 J1329+5405 is closer to its lower limit, then it too would have enough kinetic energy to be a major contributor to AGN feedback.
 3. The outflows S1 and S2 in SDSS J0936+2005 likely originate from the same material at the same distance since the velocity separation between the outflows is small and since the distances and volume filling factors are consistent within the errors.

4. The ion and line transition Cl VII 800.64 Å as well as the line transitions Ne v 480.42 Å and Ne v* 482.99 Å are first time detections.

T.M., N.A., and X.X. acknowledge support from NASA grants HST GO-14777, -14242, -14054, and -14176 as well as HST AR 15786. This support is provided by NASA through a grant from the Space Telescope Science Institute, which is operated by the Association of Universities for Research in Astronomy, Incorporated, under NASA contract NAS5-26555. T.M. and N.A. also acknowledge support from NASA ADAP 48020 and NSF grant AST 1413319. CHIANTI is a collaborative project involving George Mason University (USA), the University of Michigan (USA), and the University of Cambridge (UK).

REFERENCES

- Arav, N., Moe, M., Costantini, E., et al. 2008, *ApJ*, 681, 954-964
- Arav, N., Borguet, B., Chamberlain, C., Edmonds, D., & Danforth, C. 2013, *MNRAS*, 436, 3286
- Arav, N., Chamberlain, C., Kriss, G. A., et al. 2015, *A&A*, 577, A37
- Arav, N., Liu, G., Xu, X., et al. 2018, *ApJ*, 857, 60
- Arav, N., Xu, X., Miller, T. R., et al. 2020, *ApJS*, 247, 37
- Bahk, H., Woo, J.-H., & Park, D. 2019, *ApJ*, 875, 50.
- Borguet, B. C. J., Edmonds, D., Arav, N., Dunn, J., & Kriss, G. A. 2012, *ApJ*, 751, 107
- Borguet, B. C. J., Edmonds, D., Arav, N., Benn, C., & Chamberlain, C. 2012b, *ApJ*, 758, 69
- Borguet, B. C. J., Arav, N., Edmonds, D., Chamberlain, C., & Benn, C. 2013, *ApJ*, 762, 49
- Chamberlain, C., & Arav, N. 2015, *MNRAS*, 454, 675
- Crenshaw, D. M., Kraemer, S. B., & George, I. M. 2003, *ARA&A*, 41, 117
- Dai, X., Shankar, F., & Sivakoff, G. R. 2008, *ApJ*, 672, 108-114
- de Kool, M., Arav, N., Becker, R. H., et al. 2001, *ApJ*, 548, 609
- de Kool, M., Becker, R. H., Arav, N., Gregg, M. D., & White, R. L. 2002, *ApJ*, 570, 514
- Dere, K. P., Landi, E., Mason, H. E., Monsignori Fossi, B. C., & Young, P. R. 1997, *A&AS*, 125, 149
- Ferland, G. J., Chatzikos, M., Guzmán, F., et al. 2017, *RMxAA*, 53, 385
- Ganguly, R., & Brotherton, M. S. 2008, *ApJ*, 672, 102-107
- Green, J. C., Froning, C. S., Osterman, S., et al. 2012, *ApJ*, 744, 60
- Grevesse, N., Asplund, M., Sauval, A. J., & Scott, P. 2010, *Ap&SS*, 328, 179
- Hamann, F. W., Barlow, T. A., Chaffee, F. C., Foltz, C. B., & Weymann, R. J. 2001, *ApJ*, 550, 142
- Hewett, P. C., & Foltz, C. B. 2003, *AJ*, 125, 1784
- Hogg, D. W. 1999, arXiv e-prints, astro-ph/9905116
- Hopkins, P. F., & Elvis, M. 2010, *MNRAS*, 401, 7.
- Kaastra, J. S., Mewe, R., Liedahl, D. A., et al. 2000, *A&A*, 354, L83
- Kaastra, J. S., Kriss, G. A., Cappi, M., et al. 2014, *Science*, 345, 64
- Knigge, C., Scaringi, S., Goad, M. R., & Cottis, C. E. 2008, *MNRAS*, 386, 1426
- Korista, K. T., Bautista, M. A., Arav, N., et al. 2008, *ApJ*, 688, 108-115
- Landi, E., Young, P. R., Dere, K. P., Del Zanna, G., & Mason, H. E. 2013, *ApJ*, 763, 86
- Miller, T. R., Arav, N., Xu, X., et al. 2018, *ApJ*, 865, 90.
- Miller, T. R., Arav, N., Xu, X., et al. 2020a, *ApJS*, 247, 39
- Miller, T. R., Arav, N., Xu, X., et al. 2020b, *ApJS*, 247, 41
- Moe, M., Arav, N., Bautista, M. A., & Korista, K. T. 2009, *ApJ*, 706, 525
- Murray, N., Chiang, J., Grossman, S. A., & Voit, G. M. 1995, *ApJ*, 451, 498

- Muzahid, S., Srianand, R., Arav, N., et al. 2013, *Monthly Notices of the Royal Astronomical Society*, 431, 2885
- Proga, D., Stone, J. M., & Kallman, T. R. 2000, *ApJ*, 543, 686
- Proga, D., & Kallman, T. R. 2004, *ApJ*, 616, 688
- Reynolds, C. S. 1997, *MNRAS*, 286, 513
- Savage, B. D., & Sembach, K. R. 1991, *ApJ*, 379, 245
- Scannapieco, E., & Oh, S. P. 2004, *ApJ*, 608, 62
- Schlafly, E. F., & Finkbeiner, D. P. 2011, *ApJ*, 737, 103
- Wright, E. L. 2006, *PASP*, 118, 1711
- Xu, X., Arav, N., Miller, T., & Benn, C. 2018, *ApJ*, 858, 39
- Xu, X., Arav, N., Miller, T., et al. 2019, *ApJ*, 876, 105
- Xu, X., Arav, N., & Miller, T. 2020a, *ApJS*, 247, 38
- Xu, X., Arav, N., & Miller, T. 2020b, *ApJS*, 247, 40
- Xu, X., Arav, N., & Miller, T. 2020c, *ApJS*, 247, 42